LATE QUATERNARY GLACIER AND CLIMATE CHANGE IN THE NORTHEASTERN GREAT BASIN

A Thesis
Submitted to the Graduate Faculty
of the
North Dakota State University
of Agriculture and Applied Science

By

Jordan Rose Dahle

In Partial Fulfillment of the Requirements
for the Degree of
MASTER OF SCIENCE

Major Program:
Environmental and Conservation Sciences

March 2021

Fargo, North Dakota

North Dakota State University
Graduate School

Title

LATE QUATERNARY GLACIER AND CLIMATE CHANGE IN THE NORTHEASTERN GREAT BASIN

By

Jordan Rose Dahle

The Supervisory Committee certifies that this ***disquisition*** complies with North Dakota State University's regulations and meets the accepted standards for the degree of

MASTER OF SCIENCE

SUPERVISORY COMMITTEE:

Benjamin Laabs
Chair

Stephanie Day

Xuefeng Chu

Approved:

3/31/2021
Date

Craig Stockwell
Department Chair

ABSTRACT

This thesis presents a cosmogenic ^{10}Be exposure chronology for glacial moraines within the Baker Creek valley alongside water balance and climate modeling of Pluvial Lakes Franklin and Clover. These records further limit glacial extents and climate conditions within the Great Basin from the LGM (Last Glacial Maximum) through the subsequent deglaciation. Additionally, this thesis presents UAS-based photogrammetric analysis of the Wheeler Peak rock glacier, a modern periglacial feature in Nevada's Great Basin National park. Assessment of the volume, motion, and stability of rock glacier features is of paramount importance within the Great Basin as they are valuable hydrologic resources. Glacial moraine ages and modeled paleoclimate conditions are broadly consistent with previously published records, and through analysis of UAS-based photogrammetry, a framework for continued surveying of the Wheeler Peak rock glacier has been established.

ACKNOWLEDGMENTS

I would first like to express my sincere gratitude for the guidance and support given to me throughout my time at NDSU by Dr. Benjamin Laabs. His kindness, knowledge, and experience make him perfectly suited for the role of advisor, aiming his students in the right direction yet allowing them to find their own path. The knowledge and experience imparted to me through our work over the last two years will have a lasting impact on my life. Thanks are also due to my committee members Dr. Day and Dr. Chu, who have provided me with technical knowledge and skills that were invaluable throughout the research and writing process. Special thanks are also due to our research group members with whom I have shared many long hours in the lab and have become valuable friends. I would also like to thank the incredible network of people from my undergraduate institution, the University of Minnesota – Morris, who have supported my academic pursuits throughout the years.

DEDICATION

Johannes and Arlene Dahle

Thank you for instilling me with a thirst for knowledge, a drive for success, and for the hundreds of museum trips. You have both inspired me to be the most authentic version of myself, and I will never be able to thank you enough for all you have done to support me. As always, “I can do it myself!” but only because I know that you always have my back.

TABLE OF CONTENTS

LIST OF FIGURES

LIST OF APPENDIX TABLES

LIST OF APPENDIX FIGURES

CHAPTER 1: INTRODUCTION

The environments of the last Pleistocene glaciation have shaped much of the North American landscape, and understanding how, when, and where glaciers and large lakes existed in this landscape is key to contextualizing past climate change. The existence of large mountain glaciers in the Great Basin, a large internally drained region of southwestern North America, approximately 20 thousand years ago (ka) shows a striking contrast to the modern arid climate which dominates the interior of the region. Evidence of the last Pleistocene glaciation is recorded at the Earth surface as glacial moraines in the high mountain ranges and pluvial shoreline ridges in the expansive valleys. These landforms signify the drastically different climate which presided during the late Pleistocene, and in studying them, we can gain insight into the specific climatic conditions which would have supported these glaciers and pluvial lakes. Similarly, in studying modern periglacial features within the Great Basin, we can explore their interconnection with modern climate change.

Glacial chronologies of the Sierra Nevada (Rood et al., 2011) and Rocky Mountains (Licciardi and Pierce, 2018) have been well defined. However, one region of North America where the chronology of the last Pleistocene glaciation is still in development is the interior Great Basin of western Utah and eastern Nevada. Among the first researchers to publish observations concerning the glacial history of the Great Basin was Blackwelder (1931), who cataloged glacial deposits and landforms in valleys across the Great Basin and Eastern Sierra Nevada, categorizing moraines as Tioga (last Pleistocene glaciation) or Tahoe (penultimate Pleistocene glaciation) in age based on moraine and cirque morphology. Later, Sharp (1938) identified the last Pleistocene glaciation as “Angel Lake” and the penultimate Pleistocene glaciation “Lamoille” within the Great Basin region. Improvements to general Great Basin

glacial chronology have been made through a succession of studies, each providing more detail and context. Osborn and Bevis (2001) provide a meticulous overview of Great Basin glacial deposit morphology and discuss past publications concerning the Great Basin's glacial history. Prior to the development of cosmogenic nuclide exposure dating, glacial chronologies within the Great Basin were primarily obtained through soil development analysis and radiocarbon dating (Bevis, 1995; Wayne, 1984). The expansion of cosmogenic nuclide-based chronologies has allowed for more precise numerical age limits on glacial deposits, affording more detailed paleoclimate reconstructions of the last Pleistocene glaciation. As the Great Basin region is vast and contains numerous mountain ranges, most studies focus on improving mountain range-specific chronologies. Laabs et al. (2020) compiled moraine exposure ages from across the southwestern U.S., recalculating the reported exposure ages to improve consistency and enable inter-range comparison.

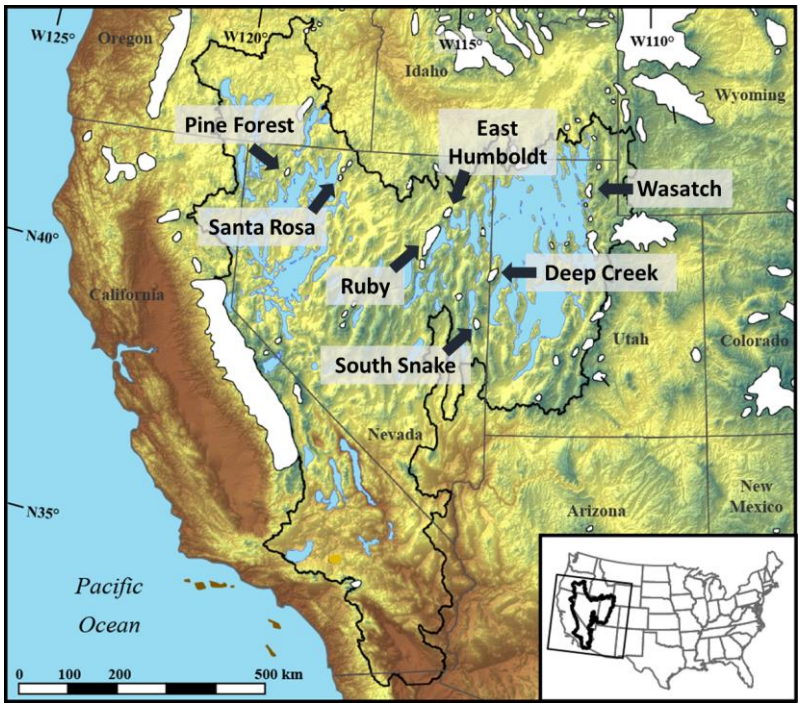

Figure 1. Shaded relief map of the southwestern U.S. with Great Basin region outlined in black. Extents of late Pleistocene pluvial lakes (Reheis, 1999) and mountain glacier systems (Pierce, 2003) within the Great Basin are shown in blue and white, respectively.

This study presents new cosmogenic nuclide exposure dating of two moraines within the Baker Creek valley of Great Basin National Park, as well as water-balance pluvial lake modeling results from Pleistocene Lakes Clover and Franklin. Exposure ages from mountain ranges throughout the Great Basin have been recalculated by Laabs et al. (2020) with uniform production rate and scaling calculation schemes, allowing for direct inter-range comparisons. Comparison to these recalculated exposure ages from moraines across the Great Basin contextualize the reported exposure ages from the Baker Creek valley (Laabs et al., 2011; Laabs et al., 2013; Laabs and Munroe, 2016; Wesnousky et al., 2016; Quirk et al., 2018; Fleming, 2019; Laabs et al., 2020). Temperature and precipitation curves resulting from pluvial lake water-balance modeling are compared to contemporaneous glacial models from adjacent mountain ranges (Truong et al., 2014; Johnson et al., 2016; Reimers and Laabs, 2018). In conjunction with one another, these models approximate a range of temperatures and precipitation factors that may have been able to sustain both the glacier and pluvial lake during a given period. Extending late Pleistocene glacial chronologies for ranges throughout the Great Basin improves the pool of available paleoclimate reference data, enabling further constraint of climatic conditions over the last Pleistocene glaciation.

The contextualization of climate change is not only a concern for the last Pleistocene glaciation, but it is also of paramount concern for modern alpine and glacial features. The arid environment of the modern Great Basin does not bring to mind visions of vast glaciers; however, it is home to a large number of postglacial and periglacial landforms. Investigation into the quantity, volume, motion, and stability of these features in the Great Basin has been lacking, and with rapidly shifting climate conditions, the longevity of these landforms is unclear. These ice-containing features are thought to play a vital role in freshwater storage within the Great Basin,

and the removal of these reservoirs from the landscape may have significant impacts on the hydrologically connected alpine environments (Millar and Westfall, 2019).

Many technological advances have allowed for data collection in new and innovative ways; one such useful technology is that of Unmanned Aerial Systems (UAS). The use of repeat UAS photography allows for efficient, low-cost, and high-frequency aerial surveying, optimal for detecting earth surface changes over time. Such technology is employed in this study to assess rock glacier motion, deformation, and volume loss. Great Basin National Park houses seven features that have been identified as rock glaciers, the most prominent of which is the Wheeler Peak rock glacier (Graham, 2014). Osborn and Bevis (2001) reported the presence of a "very small glacier" at the head of the north-facing cirque below Wheeler Peak. This glacier, consisting of a small area of exposed perennial ice at the base of the headwall, showed evidence of being capable of deforming under its own weight, allowing it to be technically considered a glacier (Osborn and Bevis, 2001). This perennial ice has recently been photographed by park staff, but it is unclear how long the perennial ice field and ice-cored rock glacier will persist. The alpine environment of the cirque, which houses the Wheeler Peak rock glacier, poses some unique challenges to effective UAS surveying. Two years of survey data have been analyzed, and the results have provided insight into specific methodologies that should be applied in the future to collect the most meaningful information.

Regional Setting

The Great Basin region of southwestern North America is an internal drainage basin located within the Basin and Range Province (Figure 1). This province, which encompasses a large portion of the southwestern United States and a smaller portion of northwestern Mexico, is characterized by North/South trending mountain ranges and broad valleys associated with

regional extension and normal faulting. The Great Basin is situated in the rain shadow of the Sierra Nevada range and primarily features desert and alpine desert ecosystems. Several mountain ranges within this region show strong evidence of past glaciations, including terminal and recessional moraines delimiting the extents of late Pleistocene valley glaciers. Osborn and Bevis (2001) discussed 29 ranges that show evidence of past glaciation within the Great Basin, exhibiting glacial features such as cirques, terminal and lateral moraines, and rock glaciers. Evidence of deglaciation and attendant hydroclimatic shifts is also preserved within the Great Basin as shoreline features of pluvial lakes, which were significantly more expansive than their glacial counterparts (Russel, 1885; Smith and Street-Perrott, 1983; Reheis et al., 2014). Pluvial lakes form within topographically closed basins during periods of increased effective moisture, and the highstands of these lakes provide climatic context similarly to glacier advances. Pluvial lakes formed within the Great Basin region at the end of the last Pleistocene glaciation; these included the well-known Lakes Bonneville and Lahontan as well as Lakes Clover and Franklin, which are of particular interest in this study (Reheis, 1999).

South Snake Range

The Snake Range situated along the Nevada/Utah border is of moderate areal extent yet features peaks of impressive height. Wheeler Peak dominates the South Snake Range, and at an elevation of 4285m, it is the second-highest peak in Nevada. This range is primarily composed of early Paleozoic quartzite, limestone, and shale with sparse granitic intrusions and zones of metamorphism (Osborn and Bevis, 2001). Great Basin National park (GBNP) located near the town of Baker, Nevada, is notable for the tourism it brings to the South Snake Range. GBNP houses the notable attractions: Wheeler peak, Lehman Caves (a Middle Cambrian age cave

system which preserved speleothem paleoclimate records; Lachniet, 2016), and the Wheeler peak rock glacier.

Alpine Glacial Features

Moraines

Moraines are glacial features constructed through the accumulation of debris deposited or deformed at the ice margin. Bennett and Glasser (2009) describe the process of moraine construction as a function of ice velocity, ice debris content, and ice retreat rate. Moraines are constructed through ablation, glaciotectonic deformation, debris dumping, or any combination of the three (Bennett and Glasser, 2009), and they represent a period of stationary ice-front position. The sediment that composes glacial moraines is called till, a diamicton or poorly sorted, unconsolidated sediment with grains ranging from silt to large cobbles and boulders. Moraines record glacial extent from terminus through recessional phases. Glacial advances generally level previously deposited moraines, meaning that moraines decrease in age moving up-valley from the terminal moraine. A terminal moraine represents the maximum extent or furthest down-valley position of a glacier during a given glaciation, forming perpendicular to the direction of ice motion due to debris deposition at the ice front. Recessional moraines are constructed during periods where the ice front is stationary, representing either a break in recession or a readvance of the glacier.

Glacial Erratics

Glacial erratics are large clasts or boulders transported and subsequently deposited by a glacier at the ice-margin. Erratics range in size, and even large erratics can be transported great distances within the glacier. Studies of erratic composition allow for the identification of provenance, origination of debris entrained by glaciers can indicate general directions of past

transport. Cosmogenic ^{10}Be exposure dating of glacial erratics allows for assessment of the duration of time in which individual boulders have been exposed to cosmic radiation. The mineral quartz is optimal for measuring cosmogenic ^{10}Be due to its high oxygen content, simple chemical composition, and stable chemical structure (Zreda and Phillips, 2000). Quartzite and granite, lithologies with high quartz content, are the predominant lithologies of glacial erratics deposited on moraines of interest in the Baker Creek valley.

Rock Glaciers

Rock glaciers are landforms that can be thought of as an endmember in the 'glacier continuum' (Anderson et al. 2018); they are lobate bodies of rock debris that insulate perennial ice and are capable of flow and deformation. They originate from either mountain glaciers that have receded and subsequently become debris-covered or ice-cored talus accumulations. Prior to a 2001 inventory of Great Basin National Park, the Wheeler Peak rock glacier was thought to be the only feature of its kind in Nevada. Since then, seven rock glaciers have been identified within the park (Graham, 2014). Recently, an inventory of the entire Great Basin Region documented 842 rock glacier features across thirteen mountain ranges. In total, 45% of these identified features were deemed to be "intact" or ice-containing and are estimated to hold a cumulative volume of approximately 0.9 km^3 of water (Millar and Westfall, 2019). The water held in these features may play an essential role as a hydrologic resource to sustain alpine, subalpine, and riparian ecosystems. As of yet, rock glacier meltwater output has not been quantified to be included in hydrologic assessments within the Great Basin (Millar and Westfall, 2019).

Figure 2. Image of Wheeler Peak rock glacier from Wheeler Peak, captured by Ben Roberts (Great Basin National Park) and taken from Graham (2014).

Pluvial Lakes

During the late Pleistocene, expansive lakes formed within low-lying valleys of the Great Basin region following the Last Glacial Maximum. These bodies of water covered vast reaches of the hydrographically closed region. Increased effective moisture during the late Pleistocene, driven by decreased regional temperature and/or increased regional precipitation, supported these

vast pluvial lakes. The shoreline ridges constructed by lakes during the Late Pleistocene record the past presence of these lakes in the now arid region. Shoreline ridges would have formed during intervals of stable water level due to back-and-forth wave motion, and dating of these shorelines allows for the development of lake-level chronologies.

Lake Clover

Shorelines indicate that at its maximum extent, Lake Clover, located in northeastern Nevada adjacent to the East Humboldt range, had a mean depth of 16 m and covered an area of approximately 800 km^2 (Munroe et al., 2020). Snow Water Lake is a modern ephemeral lake situated within the western valley of the Lake Clover basin. Current hydrologic conditions no longer support a permanent water body within this topographically closed basin. Munroe et al. (2020) conducted optically stimulated luminescence dating for a series of ten preserved shorelines in the north-central portion of the Lake Clover basin. Shorelines ranged in elevation from 1725 m to 1712 m and in age from 15.2 ± 1.5 ka to 9.5 ± 1.4 ka. The first seven preserved shorelines were constructed between 16 and 15 ka from 1725 m to 1717 m. A period of approximately 3 ka passed without further shoreline preservation before the construction of the 12 ± 1.6 and 11.5 ± 1.5 ka shorelines at 1713 m and 1715 m, respectively. The final preserved shoreline was constructed at 9.5 ka at an elevation of 1712 m. It is not possible to define Lake Clover's extent during the time intervals that lack preserved shorelines. Radiocarbon dating of fossil gastropods preserved in shoreline sediment indicates that the 1725 m shoreline had been previously occupied at 19 ka and again at 17.5 ka (Munroe and Laabs, 2013).

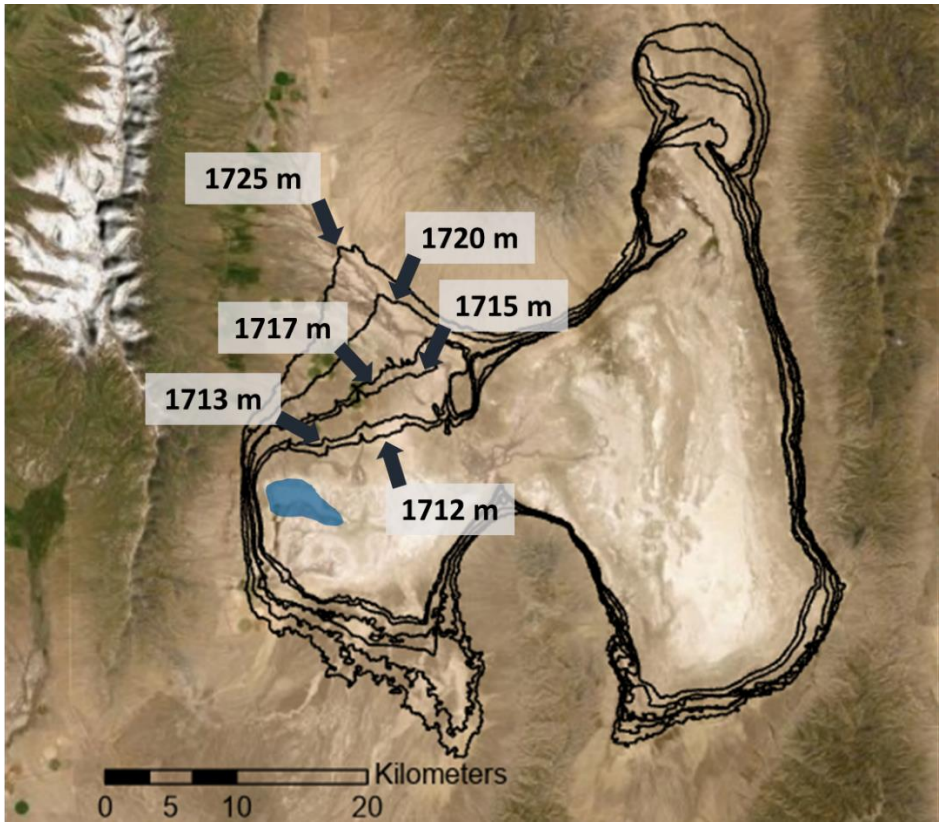

Figure 3. Satellite imagery of the Lake Clover basin with shorelines shown in black and labeled by elevation. The East Humboldt mountains are located to the east of lake basin, and the small blue water body is the approximate location of the modern ephemeral Snow Water Lake.

Lake Franklin

Southwest of Lake Clover, Lake Franklin, occupied the Ruby Valley situated directly East of the Ruby Mountains. At its highstand, Lake Franklin was approximately 36 m deep and covered an area of approximately 1100 km^2, ranking it in the top 10% of southwestern U.S. pluvial lakes by areal extent (Munroe and Laabs, 2013). The northern portion of the Lake Franklin basin was historically fed by the Franklin River, which has since been diverted, the modern body of water is now ephemeral and stream-fed (Munroe and Laabs, 2013). A perennial wetland, the Ruby Marshes, resides in the southern portion of the Lake Franklin basin and is fed by approximately 200 springs, which discharge groundwater into the marshes (Munroe and Laabs, 2013; Thompson, 1992). Munroe and Laabs (2013) employed radiocarbon dating of

aquatic gastropod shells to limit shoreline ridge ages of Lake Franklin. Three primary shoreline ridges were identified: 1830 m (20-17.3 ka), 1850 m (17.0 ka), and 1843 m (15.0 ka). Munroe and Laabs (2013) suggest that conditions held relatively stable between 20-17.3 ka, as Lake Franklin levels remained near 1830 m until the abrupt rise to highstand levels beginning around 17.3 ka. Lake Franklin reached its highstand at approximately 17.0 ka, increasing in the lake area by 168% over a span of approximately 0.5 ka. By approximately 15.0 ka, the Lake Franklin shore level receded to an elevation of 1843 m, where a prominent shoreline ridge was constructed (Munroe and Laabs, 2013).

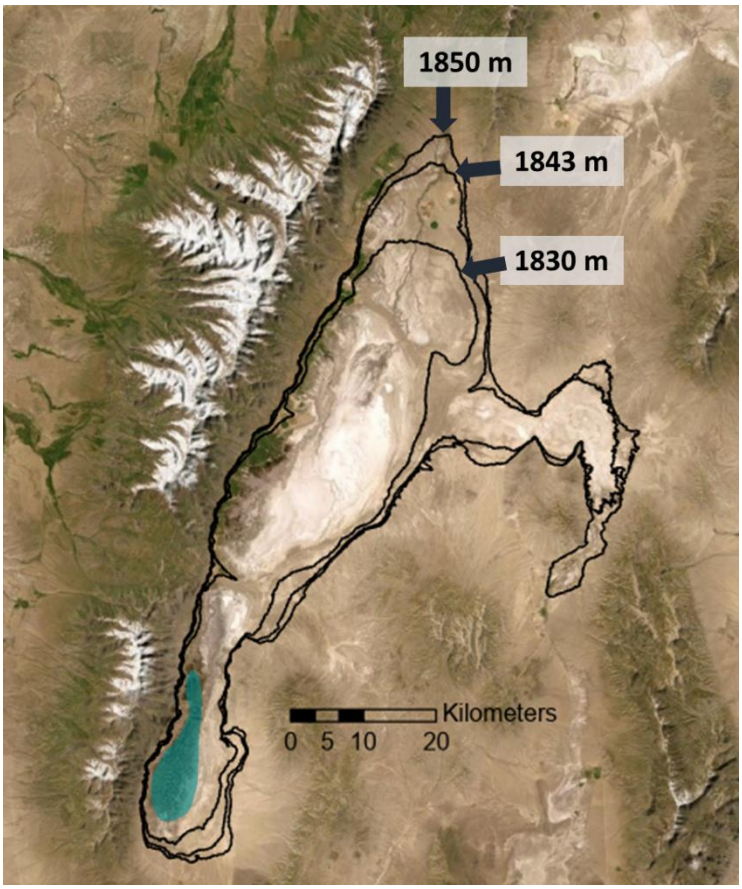

Figure 4. Satellite imagery of the Lake Franklin basin with shorelines shown in black and labeled by elevation. The Ruby Mountains are located to the East of lake basin, and the small blue water body is the approximate location of the Ruby Marsh.

Late Pleistocene Climate of the Southwestern U.S.

Significant climatic changes have occurred globally since the Last Glacial Maximum, and in the Southwestern U.S., drastic changes in hydroclimate are particularly evident through surficial landforms (alpine glacial moraines and pluvial lake shoreline ridges) and cave deposits. Existing paleoclimate records provide an invaluable framework for the interpretation of new findings. Speleothem chronologies such as those from Devils Hole (Lachniet et al., 2011), McLean's Cave (Oster et al., 2015), and Leviathan Cave (Lachniet et al., 2020) provide an isotopic record that aids in constraining modifications and potential forcing mechanisms of climate within the southwestern U.S. Cosmogenic ^{10}Be exposure dating and pluvial lake modeling results span an interval of approximately 10 kyr, from the Last Glacial Maximum (LGM) (26.5–19.0 ka; Clark et al., 2009) through Heinrich Stadial 1 (HS1) (~18.0–14.6 ka; Hemming, 2004) and into the Bölling-Alleröd interstadial (14.6–12.9 ka; Rasmussen et al., 2006). The average LGM duration reported by Clark et al. (2009) is based upon 5704 individual radiocarbon and cosmogenic nuclide exposure ages from ice sheets and mountain glaciers across the globe. The global expansion of glaciers and ice sheets to their maximum extents is thought to be in response to decreases in northern hemisphere summer insolation, tropical Pacific sea surface temperatures, and atmospheric CO_2 (Clark et al., 2009). The Heinrich Stadial 1 interval is associated with a cooling of the northern hemisphere likely due to large-scale ice discharges into the North Atlantic; these discharge events are documented by anomalous ice-rafted debris deposit (Hemming, 2004). The Bölling-Alleröd interstadial is a period of northern-hemisphere warming and regional aridification, including the Great Basin region (Munroe and Laabs, 2017); the duration of this interval has been limited by stable isotope analysis of Greenland Ice-sheet cores (Rasmussen et al., 2006).

Continuous regional hydroclimate records have been developed through isotopic analysis of speleothem deposits; regionally these records span the LGM, HS1, and subsequent time intervals of the Late Pleistocene. Analysis of the Devils Hole speleothem record, located in south-central Nevada, suggests that relatively wet conditions presided from 22.1-19.8 ka, followed by a relatively cool, dry event from 18.6 ~ 18.0 ka (Lachniet et al., 2011). Subsequently, Lachniet et al. (2011) note a transition to wetter conditions at 18.0 ka coinciding with the onset of HS1 and then warmer conditions after 16.8 ka. Growth of the Devils Hole stalactite ceased at 15.6 ka, and Lachniet et al. (2011) suggest this could be due to climatic drying. Southward displacement of the winter westerly storm track due to the presence of the Laurentide and Cordilleran ice sheets is thought to be a driver for increased winter precipitation delivery to the Great Basin during and after the LGM (Oster et al., 2015; Hudson et al., 2019). Lachniet et al. (2011) suggest that the cool, dry event (18.6–18.0 ka) may be associated with the "binge" phase of the Laurentide Ice Sheet (Clark and Bartlein, 1995), with the expansion of the continental ice sheet deflecting storm tracks southward toward the Great Basin.

Oster et al. (2015) discuss agreement of the speleothem record from McLean's Cave, located in central California, with previously published climate records. The McLean's Cave record spans from the end of the last Pleistocene glaciation, through HS1 and the Bølling-Allerød interstadial, and into the Younger Dryas. There is evidence to suggest that HS1 can be subdivided into two periods, the "Big Dry" and "Big Wet" (Broeker et al., 2009; Broeker and Putnam et al., 2012; Oster et al., 2015). The McLean's Cave record supports the hypothesis of a biphasic HS1, showing a trend from dryer conditions (17.5–16.1 ka) to wetter conditions (16.1–15.0 ka) (Oster et al., 2015). Enhanced delivery of winter precipitation due to southward deflection of the westerly storm track continues, but Oster et al. (2015) suggest that the

expansion of pluvial lakes during this interval indicates significant teleconnections between conditions in the North Atlantic and winter precipitation in the southwestern U.S.

The transition to the Bølling-Allerød is marked in the McLean's Cave record by increased $\delta^{18}O$, and $\delta^{13}C$, Oster et al. (2015) note that these changes are consistent with: (1) increased moisture from subtropical sources and/or warming, (2) decreased effective moisture and/or increased prior calcite precipitation. The McLean's Cave record also suggests a continued drying and reduction in winter precipitation throughout the Bølling-Allerød (Oster et al., 2015). This is supported by the desiccation of pluvial lakes (Munroe and Laabs, 2013; Munroe et al., 2019) and the continued recession of alpine glaciers (Fleming, 2019; Quirk et al., 2018; Reimers and Laabs, 2018). Reduction in winter precipitation delivery during the Bølling-Allerød may be related to air pressure changes in the North Pacific Ocean and a northward shift of the Pacific winter storm track (Otto-Bliesner et al., 2006; Oster et al. 2015; Lora and Ibarra, 2019).

The North American climate model Transient Climate Evolution of the Past 21 kyr (TraCE21K), presented by Lora and Ibarra (2019) aimed to assess changes in circulation, and precipitation caused by the recession of ice sheets. Model results for the southwestern U.S. indicate total warming of approximately 5° Celsius (°C) from the LGM to the Holocene, with the difference between winter add summer mean temperatures increasing throughout the deglacial period (Lora and Ibarra, 2019). Results also indicate a substantial (~50%) decrease in winter precipitation in the southwest between 15-14 ka, interrupted by a slight increase during the Bølling-Allerød (Lora and Ibarra, 2019) Lora and Ibarra (2019) also report results in the form of precipitation minus evaporation (P – E), a measure of effective moisture. Throughout the LGM and HS1 the mean annual P – E for the southwestern U.S. is positive, indicative of a hydroclimate suitable for the expansion of pluvial lakes (Lora and Ibarra). During the Bølling-

Allerød mean annual P – E decreases due to a simultaneous increase in evaporation and transition to more transient precipitation (Lora and Ibarra, 2019).

Objectives

This thesis employs existing chronologies and paleoclimate records to contextualize (1) the results of cosmogenic ^{10}Be exposure dating and (2) the results of pluvial lake modeling presented. Continued construction of chronologies for the last Pleistocene glaciation and subsequent deglaciation provides further context for limiting the timing and regional variability of climate change. Cosmogenic exposure dating of the Baker Creek valley glacier limits the timing of the local glacier maximum and the apparent pause in ice retreat of a prominent glacier in the South Snake Range. Water balance modeling of Pluvial Lakes Franklin and Clover provides a new point of comparison to assess regional hydroclimate variation throughout the last deglaciation. Finally, this thesis analyzes the utility of UAS technology in photogrammetric analysis of the Wheeler Peak Rock Glacier. Rock glaciers exhibit delayed responses to climatic change, and in the rapidly shifting modern climate of the southwestern U.S. the longevity of these hydrologically valuable features is uncertain.

CHAPTER 2: COSMOGENIC NUCLIDE EXPOSURE DATING

Introduction

In order to expand knowledge about the spatial and temporal variation in glacial recession at the end of the last Pleistocene glaciation, researchers have developed chronologies using cosmogenic nuclide exposure dating of moraine complexes. Cosmogenic nuclide exposure dating, in contrast to radiometric dating techniques used to measure the age of material directly, is a method used to calculate the length of time that material has been exposed to cosmic radiation at the surface of the Earth. Cosmic rays are high-energy particles that originate primarily from supernova events and consist of atomic nuclei, nuclear fragments, and single protons (Rossi, 1964; Gosse and Phillips, 2001; Balco, 2020). This cosmic radiation bombards the Earth atmosphere, reacting with atmospheric particles and sending cascades of secondary particles towards the Earth surface (Rossi, 1964; Balco, 2020). Some of these particles eventually impact material on the Earth's surface, creating the cosmogenic nuclides that are of interest for exposure dating geochronology. Cosmogenic nuclide measurements have applications in erosion rate, burial date computation, fault scarp formation, and the exposure dating used in this study. The use of cosmogenic nuclide methods in moraine exposure dating began in the 1990s as a new tool for constraining glacial retreat timing (Gosse et al., 1995; Phillips et al., 1990).

Production of in situ Beryllium-10 (^{10}Be), the cosmogenic nuclide of primary focus in moraine exposure age dating, occurs through spallation reactions between cosmic ray particles and oxygen atoms, where the high-energy impact fragments the atom into new cosmogenic nuclides. Quartz, a mineral of high abundance and oxygen content, is optimal for ^{10}Be exposure dating in part because of the negligible background levels of ^{10}Be present in the tight crystal

structure. The abundance and stability of quartz make it a prime target mineral for cosmogenic nuclide surface exposure dating of crystalline erratics deposited by glaciers.

The concentration of ^{10}Be within a sample is proportional to the length of time that it has been exposed at the Earth's surface. There are factors, including elevation, geographic location, topographic shielding, and erosion, that play a role in determining the rate of ^{10}Be production expected for the sample location. Elevation is used as a proxy for atmospheric depth to account for atmospheric shielding, the environmental factor with the most considerable impact on cosmogenic nuclide production rates (Balco, 2008). Cosmic ray particles lose energy with each impact, and therefore the energy available for nuclide production diminishes with depth in the atmosphere. The direction and strength of the Earth's magnetic field affect the cosmic-ray flux, decreasing the cosmogenic nuclide production rate from the poles to the equator (Balco, 2020). Production rate can then be determined based on the geographic and geometric information collected for each individual sample. Determining the length of time the erratic has been exposed at the Earth surface requires production rate scaling, involving a determination of predicted cosmic-ray interactions for a given geographical location and calibrated with cosmogenic nuclide concentrations from independently dated rock surfaces (Balco, 2020). The first task requires the summation of cosmic ray flux and energy distribution for each cosmic-ray-derived neutron that corresponds to field site characteristics, weighted by the probability that a particle of that energy level will interact with Si or O atoms in quartz (Balco, 2020). The scaling model employed for this study, "LSDn," was developed by Lifton et al. (2014) and used analytical approximations for fluxes of cosmic-ray particles, which are known to interact with the surface and produce cosmogenic nuclides. Calibration for this study relies on the *in situ* ^{10}Be production rate for Promontory Point, Utah (Lifton et al., 2015).

Early applications of cosmogenic exposure dating made vast improvements in understanding moraine ages within the White Mountains (Zreda and Phillips, 1995) and Wind River Range (Gosse, 1995), spurring interest in this promising new method of moraine chronology. Standardization of laboratory practices (Gosse et al., 2001; Corbett et al., 2016) and improvements to production-rate scaling (Lifton, 2014) and calibration have improved researchers' ability to measure cosmogenic nuclides at lower concentrations and with more certainty. Exposure ages of moraines and other surficial deposits can now be computed with a measurement uncertainty of approximately 2-4% (Balco, 2020).

Ranges in the Great Basin, including the South Snake range, have historically lacked thorough chronology from the last Pleistocene glaciation. Recent studies, however, have successfully applied cosmogenic nuclide dating methodology to moraine complexes in mountain ranges, including the Ruby Mountains, Santa Rosa, and Pine Forest, and have helped fill this gap (Fleming, 2019; Laabs et al., 2013). Results from these studies have found that recession timing within the Great Basin is broadly synchronous with chronologies developed for the Sierra Nevada and Rocky Mountains at the end of the last Pleistocene glaciation (Laabs et al., 2013). Both studies identify two distinct moraine ages: terminal moraines (approximately 21-20 ka) coinciding with the latter portion of the last Pleistocene glaciation and recessional moraines (approximately 18-17 ka) coinciding with the Heinrich Stadial 1 event (Hemming, 2004; Fleming, 2019).

This study expands the chronology available for the Great Basin by obtaining surface-exposure ages for a set of moraines within Great Basin National Park. In 2018, samples were collected from two moraines within the Baker Creek valley southeast of Baker Peak. Continued construction of glacial chronologies for the last Pleistocene glaciation provides further context

for the timing and variation of climate change during the transition from the LGM to Heinrich Stadial 1. Cosmogenic exposure dating of the Baker Creek valley glacier limits timing of the local glacier maximum and the apparent pause in ice retreat. The ages of the sampled moraines will help continue to construct a chronology of glacial recession at the end of the Last Pleistocene Glaciation and provide further context to the timing and variation of accompanying climate change.

Methods

Field Methodology

Sampling conducted within Great Basin National Park focused on the Late Pleistocene terminal and recessional moraines of Baker Creek valley to limit the timing of maximum ice extent and subsequent retreat in the South Snake Range. In 2017, fifteen samples were collected from the terminal moraine representing the glacier's maximum late Pleistocene extent. Subsequently, in 2018, six samples were collected from a recessional moraine, deposited when the glacier in Baker Creek valley receded to approximately 50% of its maximum glacial extent. Glacial erratics targeted for sampling are quartz-rich granite and quartzite boulders situated at or near the crest of the moraine. The collection of these samples follows procedures standard for cosmogenic nuclide exposure dating studies (Gosse and Phillips, 2001). A sample mass of approximately 1 kg is removed from the surface of the erratic with a portable rock saw, sledgehammer, and chisel. Samples are collected to a depth of 1.5-2 cm; attention to sample depth is necessary due to the rapid decrease of cosmogenic nuclides produced below the rock surface. Production rate is dependent on many factors, as discussed above, so the selection of suitable targets must take each into consideration. Gosse and Phillips (2001) provide a thorough discussion of considerations that must be accounted for when selecting an erratic for sampling.

Factors of primary importance are surface geometry and lithology; the sampling surface should be large enough to prevent edge effects and flat enough to prevent self-shielding (Gosse and Phillips, 2001). When a suitable erratic has been selected and sampled, geographic and geometric data must be recorded, including latitude, longitude, elevation, sample height, and topographic shielding. Topographic shielding concerns obstructions that inhibit cosmic radiation reaching the sampled surface, such as mountain peaks, ridges, or valley walls. Shielding features are recorded as the angle above the horizon and azimuth for the whole 360-degree viewshed. Accurate recording of this information is key to production rate calculation and result reproducibility.

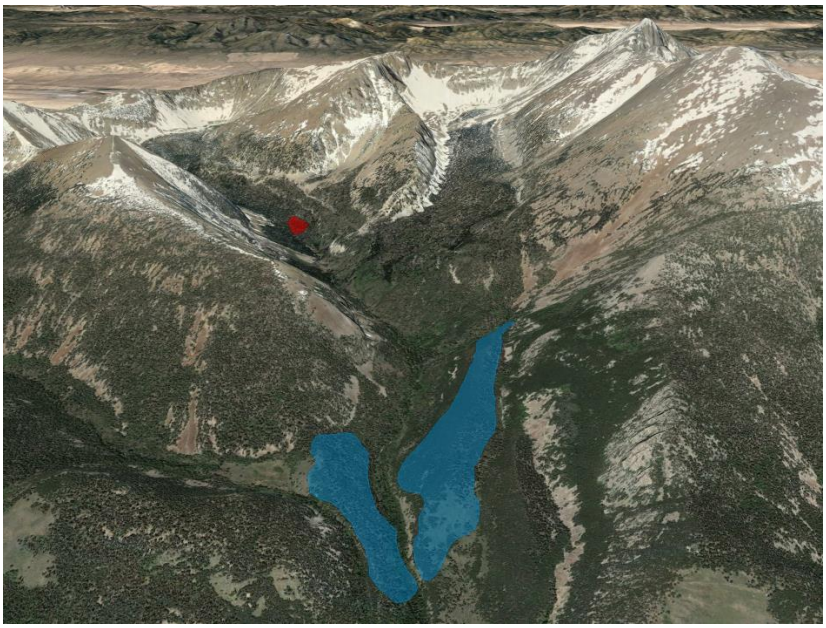

Figure 5. Oblique satellite image from Google Earth of the Baker Creek valley with lateral moraines highlighted in blue and recessional highlighted in red.

Laboratory Methodology

Each moraine-boulder sample from the Baker Creek valley was processed through the NDSU Cosmogenic Nuclide Preparation Lab to first mechanically and then chemically prepare the samples for AMS analysis. The preparation methodology used in the lab was adapted from Laabs et al. (2013). Each rock sample is crushed and milled to a target grain size of 250 to 500

microns using a jaw crusher and a disk mill. The sample fraction of the target grain size is separated by sieve but can consist of more than the target mineral species. Quartz must then be isolated from other mineral species naturally present in the sampled erratic. The first step in isolating quartz is to remove magnetic grains with a neodymium magnet, then rinsing and decanting with deionized water removes dust and mica grains. These are simple yet extremely efficient ways to remove unwanted material. The final mechanical quartz isolation method is froth flotation, a procedure in which felsic grains are removed by taking advantage of the increased rate at which CO_2 gas bubbles adhere to felsic grain surfaces (Whelan and Brown, 1956). Samples are prepared for flotation by etching in dilute hydrofluoric acid (HF), altering the grain surface textures to make quartz hydrophilic and feldspars hydrophobic (Sulaymonova et al., 2018).

The final stages of quartz purification are chemical etching in 6N hydrochloric acid (HCl) followed by etching in 1-5% hydrofluoric acid (HF) and nitric acid (HNO_3). HCl etching bleaches the quartz grain surfaces and removes Fe-oxide coatings. Further etching in dilute HF/HNO_3 targets lingering feldspar and mica grains, removes any meteoric Be from grain surfaces and reduces grain size to ensure that no polymineralic grains remain. To ensure that the samples consist of purified quartz and ready for AMS preparation, they must pass a dissolution test.

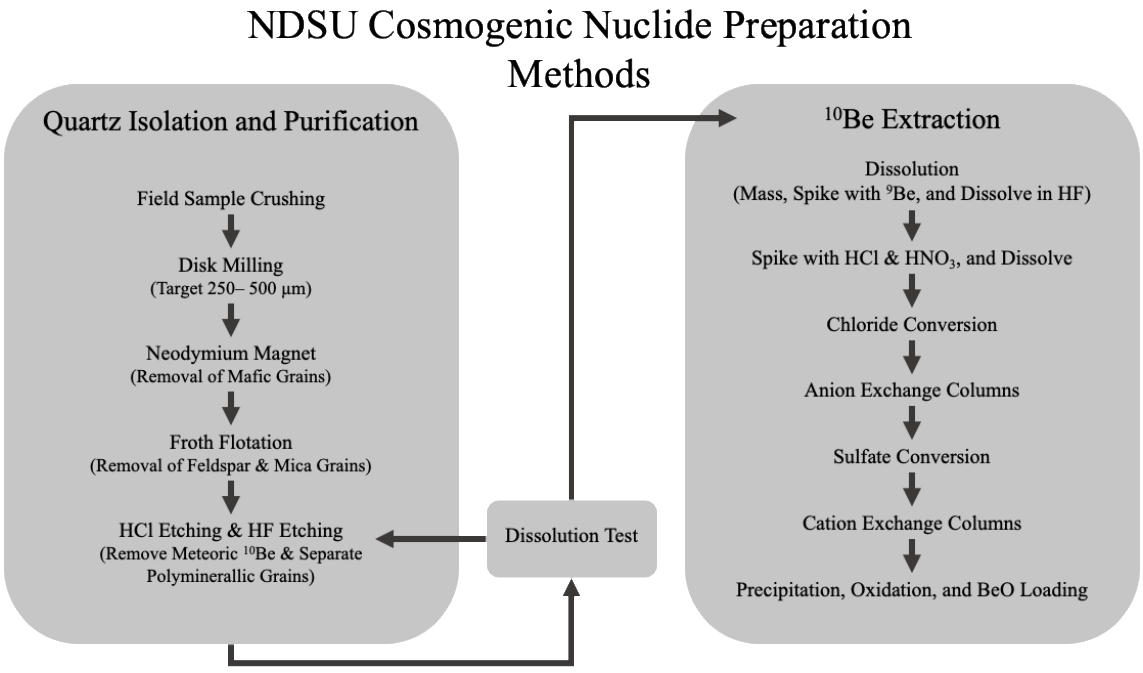

Figure 6. Schematic of NDSU cosmogenic nuclide preparation laboratory methodology. Quartz isolation procedures are shown on the left, and ^{10}Be extraction procedures are shown on the right.

Once the samples have all passed the dissolution test, chemical preparation for AMS analysis may begin. Samples must be processed from pure crystalline quartz, isolating Be in the form of BeO. This is accomplished through a series of chemical conversions and column chromatography. A complete schematic of laboratory procedures is shown in Figure 6, and a detailed description of laboratory methodology is provided in Appendix A. Isolated BeO is then loaded into cathodes and shipped to the AMS facilities at the Purdue University PRIME lab.

Age Calculations

AMS results received from the PRIME lab are in the form of ^{10}Be/^{9}Be ratios; this is standard for AMS analysis as absolute nuclide counts are difficult and would likely not reflect the actual number of target nuclide atoms present in the sample (Muzikar, 2003). In order to determine this ratio, prepared samples are negatively ionized and propelled along a beam line by electric and magnetic fields (Muzikar, 2003). Unwanted nuclides are either removed before the

sample reaches the detector or recognized by the detector as an unwanted signal. The target nuclide and its corresponding stable isotope are detected, and the ratio is calculated (Muzikar, 2003). Once returned, $^{10}Be/^{9}Be$ ratios are converted into ^{10}Be concentrations in atoms per gram of quartz for each sample. These concentrations of ^{10}Be, in conjunction with sample geography and site geometry, allow for the computation of surface exposure ages using a production scaling calculation. Exposure ages for the samples are calculated using the Version 3 online exposure age calculator (formerly known as the CRONUS-Earth calculator) hosted by the Cosmogenic Nuclide Lab at the University of Washington (Balco et al. 2008). The Version 3 calculator uses a computational methodology from Balco et al. (2008) and provides an option of three production rate scaling methods. Production rate models from Borchers et al. (2016) and Lifton et al. (2015) were employed for global and local (Promontory Point, Utah) production rate calibration, respectively. The Version 3 calculator also employed the Lifton-Sato-Dunai (LSDn) scaling model from Lifton et al. (2014). The resulting output from the Version 3 Calculator includes both "internal" and "external' uncertainty. Internal uncertainty is dependent solely on the measurement error for nuclide concentration, where external error also considers production rate and scaling uncertainty (Balco et al., 2008). Internal uncertainty is generally only used when comparing individual sample ages from the same field site, calculated with the same production rate and scaling models. External uncertainty is appropriate for comparisons with any other geologic age.

Results

Cosmogenic nuclide exposure ages were computed for ten terminal moraine samples and six recessional moraine samples from the Baker Creek valley in Great Basin National Park. The terminal moraine samples range in age from 18.4 ± 0.9 to 22.1 ± 1.2 ka. The recessional moraine

samples range in age from 12.3 ± 0.8 to 15.0 ± 1.6 ka. Individual sample ages are reported in Table B2, where each exposure age is reported along with both internal and external uncertainty.

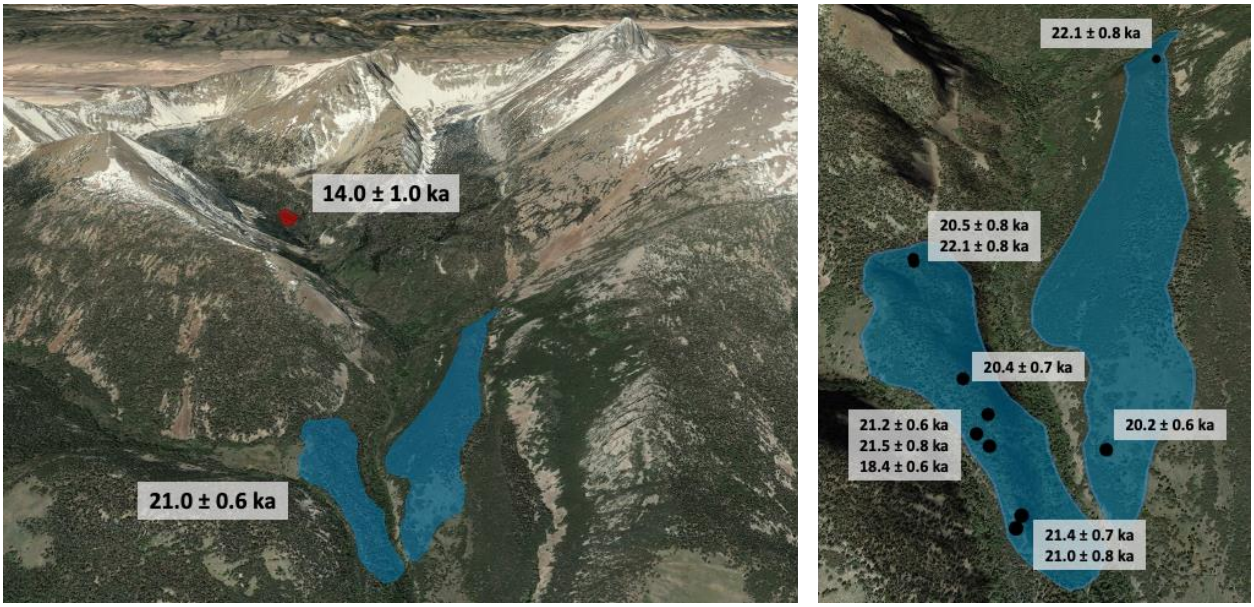

Figure 7. Average cosmogenic ^{10}Be exposure ages from Baker Creek valley lateral and recessional moraines are shown to the left. On the right, individual exposure ages from the LGM age lateral moraines are shown at their respective sampling locations. Satellite imagery obtained from Google Earth.

Following Balco (2011), the distribution of the sample ages was analyzed by computing the reduced chi-squared statistic. The reduced chi-squared value is used to identify the source of variation within the sample age sets and identify outliers; a value near 1.0 would indicate that measurement uncertainty is likely responsible for observed variation (Balco, 2011). The Baker Creek terminal moraine has one sample with an exposure age of 18.4 ± 0.9 ka, which is approximately 2 kyr younger than the remaining sample exposure ages. This sample does not agree within uncertainty with the other nine terminal moraine samples and is therefore considered an outlier. When the reduced chi-squared is calculated for the complete set of terminal moraine samples, the result is a value of 2.7; when the individual exposure age of 18.4 ± 0.9 is removed from the calculation, the resulting value is reduced to 0.9. The recessional

moraine has a reduced chi-squared value of 2.5, with one sample aged approximately 1 kyr younger than the other four. Recessional moraine samples all agree within uncertainty with at least one other sample in the set, so the exclusion of the youngest sample would not be justified. The distribution of exposure ages from both moraines is displayed as violin plots with their respective reduced chi-squared values reported in the lower-left corner (Figure 8).

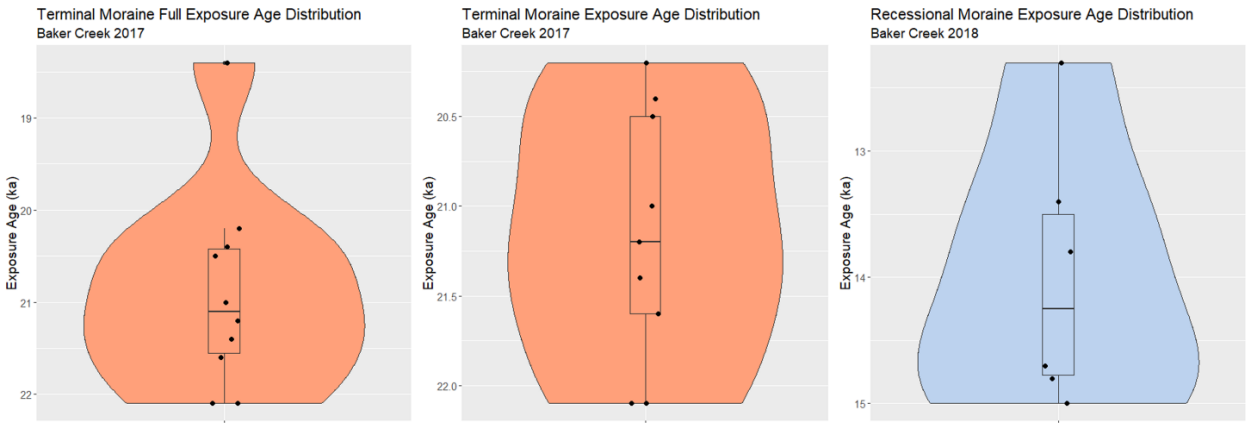

Figure 8. Distribution of sample ages from lateral and recessional moraines of the Baker Creek valley. Violin plots are overlain by box and whisker plots for each set of ages.

Discussion

The glacial chronology of the Great Basin has been dramatically improved due to the diligent work of researchers through cosmogenic exposure dating of alpine valley glacier moraines. Results from previous studies of glacial chronologies in the Great Basin are presented here, along with the Baker Creek valley results to provide regional context. The regional results presented are from studies conducted in the Wasatch (Laabs et al.,2011; Laabs and Munroe, 2016; Quirk et al., 2018), Ruby Mountain (Laabs et al.,2013; Wesnousky et al.,2016), East Humboldt (Laabs et al., 2020), South Snake (Laabs and Munroe, 2016), Deep Creek (Laabs and Munroe, 2016), Santa Rosa (Fleming, 2019), and Pine Forest Ranges (Fleming, 2019). Cosmogenic nuclide exposure ages reported in the aforementioned studies have been

recalculated by Laabs (2020) for ease of intercomparison, and the recalculated exposure ages are plotted along with the new Baker Creek exposure ages in Figure 9. These studies identify three moraine age populations: terminal moraines associated with the latter portion of the Last Glacial Maximum (21-20 ka), down-valley recessional moraines coinciding with the onset of Heinrich Stadial 1 (18-14.6 ka), and up-valley recessional moraines associated with readvance or breaks in recession during the ~15-13 ka interval (Laabs et al., 2020; Marcott et al., 2019). Down-valley and up-valley moraines are distinguished from one another by Laabs et al. (2020) based on geomorphic position. Recessional moraines are considered to be down-valley if they represent a glacier length ≥ 75% of the known maximum extent; those that represent a glacier length of < 75% of LGM extent are considered up-valley.

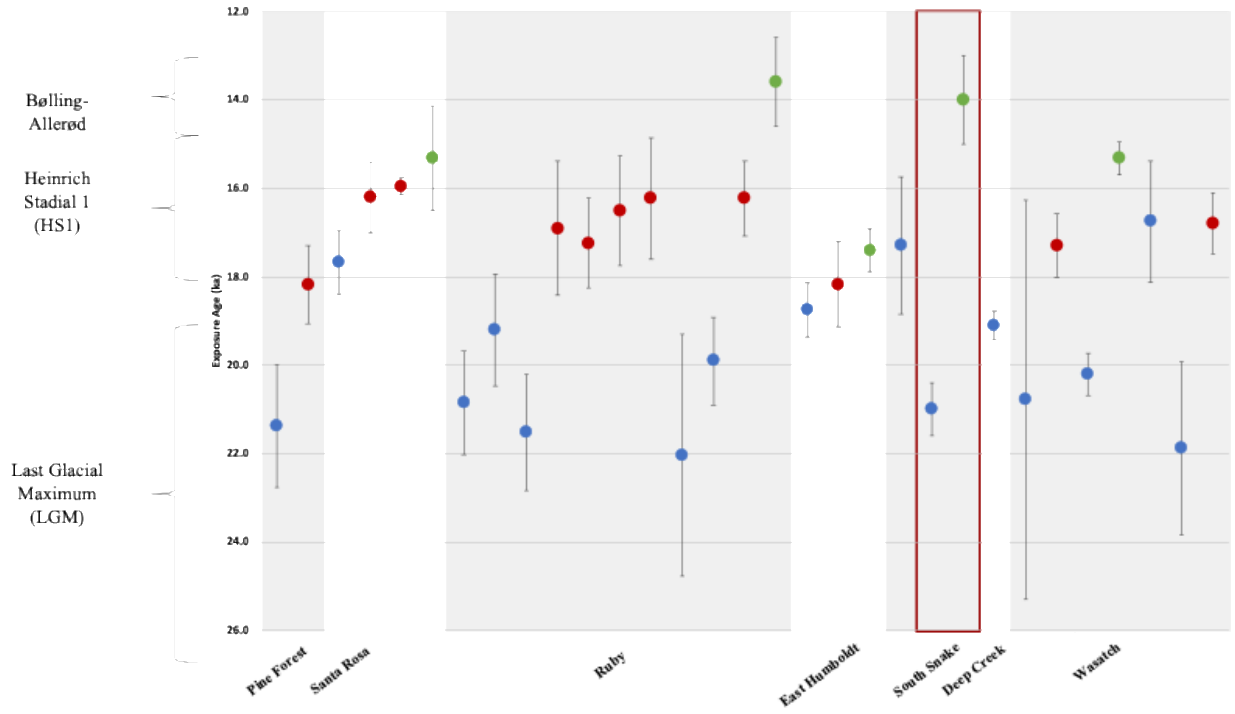

Figure 9. Comparative plot of terminal (blue), down-valley recessional (red), and up-valley recessional (green) moraine ages from select ranges throughout the Great Basin region. The moraine ages presented for the Baker Creek valley are outlined in red. Data shown in this figure are from studies conducted in the Wasatch (Laabs et al.,2011; Laabs and Munroe, 2016; Quirk et al., 2018), Ruby Mountain (Laabs et al.,2013; Wesnousky et al.,2016), East Humboldt (Laabs et al., 2020), South Snake (Laabs and Munroe, 2016, This Thesis), Deep Creek (Laabs and Munroe, 2016), Santa Rosa (Fleming, 2019), and Pine Forest Ranges (Fleming, 2019).

Laabs et al. (2020) summarized the glacial chronology of the southwestern U.S., reporting a region-wide average terminal moraine exposure age of 19.5 ± 2.3 ka and average down-valley recessional exposure age of 17.0 ± 1.8 ka. The Baker Creek valley terminal moraine has a mean age of 21.0 ± 0.6 ka after the exclusion of the 18.4 ka sample. This exposure age falls in line with expectations based on exposure ages of other terminal moraines in the region. The Baker Creek valley recessional moraine has an average sample age of 14.0 ± 1.0 and represents a recession to approximately 50% of the glacier's known maximum extent; therefore, this is moraine will be referred to as an up-valley recessional moraine. Few up-valley recessional moraine ages are available within the Great Basin; however, the Baker Creek valley recessional

moraine agrees within uncertainty with up-valley recessionals from the Santa Rosa and Wasatch ranges (Fleming, 2019; Quirk et al., 2018).

Fleming (2019) presented exposure ages from Blue Lake in the Pine Forest Range of northwestern Nevada and from Granite Peak in the Santa Rosa range of northcentral Nevada. Terminal and recessional moraines in the Pine Forest range were dated to 21.4 ± 1.4 ka and 18.2 ± 0.9 ka, respectively (Fleming, 2019). Fleming (2019) sampled four moraines in the Santa Rosa range aged 17.7 ± 0.7 ka, 16.2 ± 0.8 ka, 16.5 ± 0.2 ka, and 15.3 ± 1.2 ka. The terminal moraine from Blue Lake agrees with the presented Baker Creek terminal moraine age, while the oldest moraine from the Santa Rosa range is approximately 3 kyr younger. The presented up-valley recessional moraine from Baker Creek is consistent with the final recessional moraine from Granite Peak; however, the margin of overlap is narrow.

Laabs et al. (2013) computed cosmogenic exposure ages for a series of seven moraines in the Seitz Canyon of the Ruby Mountains, located in northeastern Nevada. Laabs et al. (2020) recalculated the ages of the Seitz Canyon moraines and grouped the three oldest as the "terminal" age moraines and the four youngest as "down-valley" recessional moraines; their averaged ages are 20.5 ± 1.0 ka and 16.7 ± 0.4 ka respectively (Laabs et al., 2020). Additionally, Wesnousky et al. (2016) dated the terminal moraine in Hennen Canyon in the western Ruby Mountains, resulting in a mean exposure age of 22.0 ± 2.7 ka. Terminal moraines from both Seitz and Hennen Canyons are consistent with what has been presented for the Baker Creek terminal.

Munroe et al. (2015) computed cosmogenic nuclide exposure ages for two moraines at Angel Lake in the East Humboldt Range, the type locality for the last Pleistocene glaciation within the Great Basin (Sharp, 1938). The terminal moraine at Angel Lake was dated to 18.8 ±

0.6 ka, and the recessional moraine was dated to 18.2 ± 1.0 ka (Munroe et al., 2015; Laabs et al., 2020). These moraine ages fall nearly directly between the Baker Creek terminal and recessional moraine ages presented, agreeing with neither.

Laabs and Munroe (2016) computed ^{10}Be cosmogenic ages for sites including Granite Creek in the Deep Creek Range and Dead Lake in the South Snake Range. Both the Deep Creek and South Snake ranges are located centrally along the Nevada-Utah border. The terminal moraine from Granite Creek was dated to 19.1 ± 0.3 ka, and the terminal moraine from Dead Lake was dated to 17.3 ± 1.6 ka (Laabs and Munroe, 2016; Laabs et al., 2020). The Baker Creek terminal moraine does not coincide with the terminal moraine ages from Granite Creek or Dead Lake, though Dead Lake and Baker Creek reside in the same range. The average ^{10}Be exposure age of the Baker Creek terminal is based on a more robust set of individual exposure ages than the Dead Lake terminal moraine.

Recalculated cosmogenic nuclide exposure ages from the Wasatch range, located in northcentral Utah, are included in this comparison as an eastern boundary to the Great Basin region. Laabs and Munroe (2016) also dated Bells Canyon terminal and recessional moraines, 21.9 ± 2.0 ka, and 16.8 ± 0.7 ka, respectively. Quirk et al. (2020) reported ^{10}Be exposure ages for a terminal and recessional moraine in Big Cottonwood Canyon, with average exposure age of 20.2 ± 0.5 ka and 15.3 ± 0.4 ka, respectively. Laabs et al. (2011) reported ^{10}Be exposure ages for terminal moraines in the American Fork Canyon (16.8 ± 1.4) and Little Cottonwood Canyon (20.8 ± 4.5 ka), and a recessional moraine in Little Cottonwood Canyon (17.3 ± 0.7) (Laabs et al., 2020). The Baker Creek terminal moraine ^{10}Be exposure age agrees with the terminal moraine ages from Bells, Big Cottonwood, and Little Cottonwood Canyons. The Baker Creek

up-valley recessional moraine is narrowly in agreement with the recessional moraine from Big Cottonwood Canyon.

Beyond the Great Basin, the climate of the latter portion of the last Pleistocene glaciation is well constrained in the Rocky and Sierra Nevada Mountains. Summarized by Laabs et al. (2020), ^{10}Be exposure ages for terminal moraines in the Sierra Nevada generally fall between 21-18 ka, and down-valley recessional moraines generally fall between 17-15 ka. The Rocky Mountain moraine ages mirror the intervals from the Sierra Nevada but fall a millennium earlier (22-18 ka, and 18-16 ka for terminal and recessional, respectively) (Laabs et al., 2020).

Conclusion

The Baker Creek valley terminal moraine average exposure age of 21.0 ± 0.6 ka agrees with other regional LGM terminal moraine ages and with the cool climate conditions inferred from regional paleoclimate records. The regional average LGM terminal moraine age of 19.5 ± 2.3 ka coincides with the global expansion of glaciers and ice sheets to their maximum extents due to decreases in northern hemisphere summer insolation, tropical Pacific sea surface temperatures, and atmospheric CO_2 (Clark et al., 2009). The Baker Creek valley recessional moraine exposure age of 14.0 ± 1.0 ka aligns with the up-valley recessionals from the Wasatch and Santa Rosa as well as bedrock exposures from the Ruby Mountains (Quirk et al., 2018; Fleming et al., 2019; Laabs unpublished). Generally, recessional moraines dated within the Great Basin have coincided with the onset of HS1 and the expansion of pluvial lakes (Laabs et al., 2020). Southward displacement of the winter westerly storm track due to the presence of North American ice sheets is thought to be a driver for increased winter precipitation delivery to the Great Basin during HS1 (Oster et al., 2015; Lora and Ibarra, 2019). The subsequent Bølling-Allerød interstadial is a period of warmer and drier conditions related to an enhanced Aleutian

Low and northward deflection of the Pacific winter storm track (Otto-Bliesner et al., 2006; Oster et al. 2015; Lora and Ibarra, 2019). The up-valley recessional moraine from Baker Creek suggests that some alpine mountain glaciers were able to persist at moderate extents until the beginning of the Bølling-Allerød interstadial and until after pluvial lakes began to fall.

CHAPTER 3: WATER BALANCE MODELING OF PLUVIAL LAKES

Introduction

The climatic shifts during the final stages of the last Pleistocene glaciation are recorded by pluvial lake shorelines and the previously discussed glacial moraines. Preserved shorelines from pluvial lakes throughout the Great Basin have been cataloged, and when dated, can provide a chronology of lake-level changes, some of which occurred in step with changes in mountain glacier lengths. Both glacier and pluvial lake extents are dependent on climate, expanding and receding as conditions vary. Numerical modeling of both glaciers and pluvial lakes must distill complex environmental processes into representative computations, allowing for approximating the climatic conditions that could have supported the existence of the lake or glacier at a given extent. Using a modified version of the lacustrine regression model developed by Condom et al. (2004) for modeling large, ancient lakes to infer paleoclimate conditions, it is possible for us to estimate paleoclimatic conditions in valleys of the Great Basin where pluvial lakes existed downstream of mountain glaciers at the end of the Last Pleistocene Glaciation.

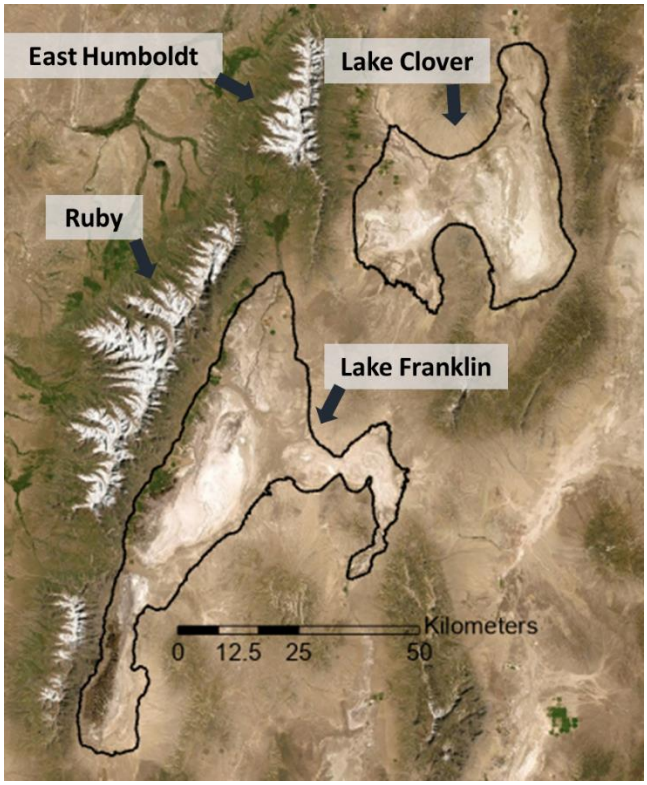

Figure 10. Labeled location map for pluvial Lakes Clover and Franklin. Highstand shorelines of Lakes Clover and Franklin are shown in black (Munroe et al., 2020; Munroe and Laabs, 2013).

Condom et al. (2004) developed a water balance model that applied modern basin characteristics, temperature, precipitation, and solar insolation to approximate the climatic conditions which suitable to support a paleo-lake of interest. The original application of this model by Condom et al. (2004) aimed to evaluate the relationship between climate change and lake-level variations in the Andean Altiplano of South America. Past application of this methodology within the Great Basin region by Fleming (2019) modeled two phases of Lake Franklin using a slightly modified version of the Condom et al. (2004) model with a locally calibrated evaporation scheme. Model results presented here represent a further modification of the Condom et al. (2004) water balance model by Belanger et al. (2019). This model is designed to estimate modern soil water capacity (CapaS) from modern monthly meteorological data, avoiding the uncertainty associated with estimating runoff in a high water-use basin. The CapaS

value is iteratively computed based on the monthly meteorological data and lake area. For the purpose of understanding paleo-environmental conditions, we assume that the modern CapaS value is a reasonable approximation for the CapaS of the watershed during the Pleistocene.

Pluvial lakes Clover and Franklin are located in northeastern Nevada, situated directly east of the East Humboldt and Ruby Mountains, respectively (Figure 10). Lake Clover covered an area of 740 km^2 at its highstand, occupying more than 25% of its watershed area. Munroe et al. (2020) recently published optically stimulated luminescence (OSL) ages for a suite of shorelines from Lake Clover, which provide a chronological framework for the lacustrine regression modeling. A series of ten shorelines located at 1725, 1724, 1723, 1721, 1720, 1718, 1717, 1715, 1713, and 1712 meters were identified through topographic surveying (Munroe et al., 2020). The ten identified shorelines range in age from 15.9 ± 1.9 ka at the highstand to 9.5 ± 1.4 ka at the lowest elevation shoreline. Shoreline elevations in Lake Clover show strong temporal agreement with chronologies of similar pluvial lakes within the Great Basin. The highstand was constructed during the late stages of Heinrich Stadial I, followed by progressive lake level decreases through the subsequent 1000 years. There is a notable gap in constructed shorelines between ~15 and 12 ky BP, during which the level of Lake Clover is unknown. Shorelines dated to ~11.5 to 12 ky BP are thought to correlate to a slight lake level rise during the Younger Dryas, and finally, the lowest stable lake level is dated to ~9.5 ka BP (Munroe et al., 2020). This chronological framework was used to model the climatic conditions required to sustain Lake Clover at the known lake levels.

Southwest of Lake Clover, the Lake Franklin basin, is situated directly east of Nevada's Ruby Mountains. Munroe and Laabs (2013) employed radiocarbon dating of aquatic gastropod shells as a means of limiting pluvial beach ridge ages of Lake Franklin. Three primary shoreline

ridges were identified: 1830 m (20-17.3 ka), 1850 m (17.0 ka), and 1843 m (15.0 ka). Munroe and Laabs (2013) suggest that conditions held relatively stable between 20-17.3 ka, as Lake Franklin levels remained near 1830 m until the abrupt rise to highstand levels beginning around 17.3 ka. Lake Franklin reached its highstand at approximately 17.0 ka, increasing the lake area by 168% over a span of approximately 0.5 ka (Munroe and Laabs, 2013). By approximately 15.0 ka, Lake Franklin level receded to an elevation of 1843 m, where a prominent shoreline ridge was constructed. Shorelines of Pleistocene Lake Franklin were modeled at elevations of 1830 m (20 ka), 1850 m (17 ka), and 1843 m (15 ka).

Methods

The model used for this analysis has been adapted by Belanger et al. (2019) from the original water balance model developed by Condom et al. (2004), improving uncertainty constraints in model solutions and enabling application of the model in the Great Basin region. The water balance model is designed with two reservoirs, the watershed, and the lake, which are connected through soil recharge. This model is designed specifically for closed basin systems, making it optimal for application in a pluvial lake environment, as seen in the cases of Lakes Clover and Franklin. The model used by Fleming (2019) for modeling Lake Franklin had been adapted by Steen et al. (2015) from the original Condom (2004) methodology. Specifically, Steen et al. (2015) modified the potential evaporation equation's coefficient to represent the Great Basin environment.

In water balance equation adapted from Condom et al. (2004) (Eq. 1) the volume of the lake for any given time interval is dependent on the precipitation (PLake, PWS), evaporation (EPLake, EtWS), and area (ALake, AWS) of the lake and the watershed, the time steps for input data are seasonal (three-month) intervals.

$$\frac{dV_{Lake}}{dt} = (P_{Lake} - EP_{Lake})A_{Lake} + (P_{WS} - Et_{WS})A_{WS} \quad \text{(Eq. 1)}$$

The first computation necessary is the determination of a coefficient representing modern soil water capacity, CapaS. Modern precipitation, temperature, and insolation data were obtained from PRISM Climate Group of Oregon State University; insolation was corrected for topography using equations from Plummer and Phillips (2003). These data are converted to 800-meter raster grids using ArcGIS software. Coded grids are created for each dated Lake Clover shoreline, with each cell in the grid assigned to either: 1 (modern lake), 2 (paleo-lake), or 3 (watershed). For each Lake Clover shoreline elevation, the precipitation, temperature, and insolation grids are compiled into a single MATLAB file consisting of matrices for each timestep and one for the coded raster. This file will be the foundation of CapaS computation and paleo-lake modeling.

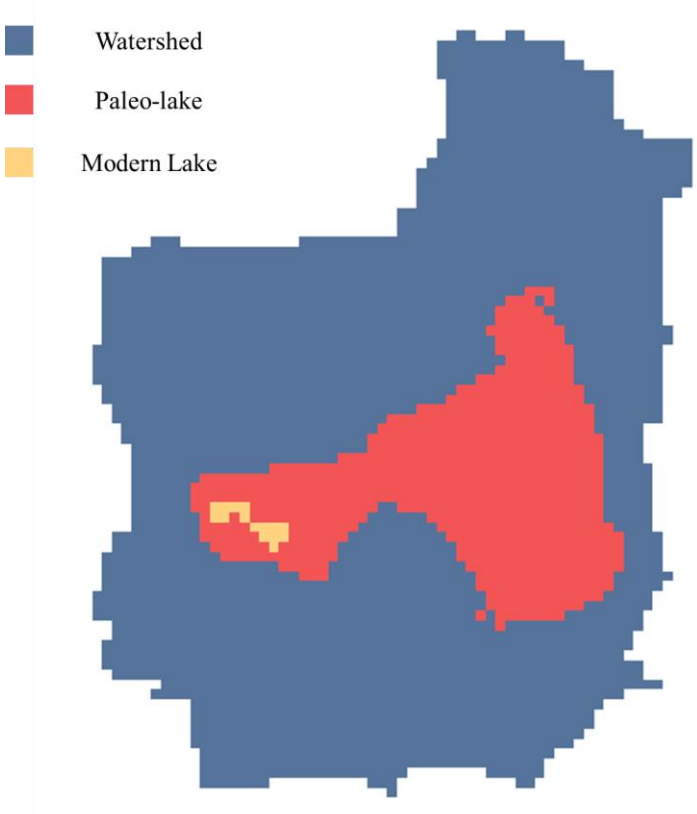

Figure 11. Example of coded raster input for water balance modeling procedures. Watershed area (blue), paleo-lake area (red), and modern lake area (yellow) represent an extent of Lake Clover.

Now that matrices have been compiled, computation of CapaS begins by calculating total precipitation and evaporation for the lake area. Total lake precipitation is a summation of precipitation for all cells coded as "modern lake." The calculation of total lake evaporation requires more careful consideration and is crucial because it provides the only source of model validation (Fleming, 2019). There is a thoughtful discussion of appropriate potential evaporation computation for pluvial lake basins in the Great Basin region in Fleming (2019). Potential evaporation is calculated using the equation below, which was published by Steen et al. (2015) as an adaptation of the potential evaporation equation given by Condom et al. (2004).

$$EP = \frac{Rg}{\lambda}(T + 17.8)0.0382 \quad \text{(Eq. 2)}$$

In equation 2, *T* is the mid-month air temperature, and λ is the latent heat. The sole modification was to change the coefficient from 0.0145 to 0.0382 (Steen et al., 2015). The term *Rg* in this equation is the total solar radiation, and it is given by equation 3, where *Re* is mid-month extraterrestrial radiation based on latitude, *Suntr* is the number of actual mid-month daylight hours, and *Sunth* is the number of mid-month astronomical daylight hours.

$$Rg = \left(a + b\left(\frac{Sun_{tr}}{Sun_{th}}\right)\right)Re \quad \text{(Eq. 3)}$$

Total precipitation over the watershed area is, similar to that of the lake area, a summation of precipitation for all cells coded as "watershed" and "paleo-lake." Both categories must be included in this summation because the CapaS calculation does not consider the paleo-lake area. Total evapotranspiration for the watershed area is computed based on soil water availability, where the following equations from Condom et al. (2004) are solved iteratively to identify an appropriate CapaS for the watershed.

$$Etws_{n+1} = \left(\frac{Hws_n}{CapaS}\right) * \left(2 - \frac{Hws_n}{CapaS}\right) * EP_{n+1} \quad \text{(Eq. 4)}$$

$$Hws_{n+1} = Hws_n + Pws_{n+1} - Etws_{n+1} \quad \text{(Eq. 5)}$$

The value *Hws* is equal to the soil's actual water content in a given grid cell and must be set to an initial value to initiate the model run. After a maximum of 10 annual iterations, the water balance calculations converge on a value for CapaS, representing the water soil capacity for the modeled lake level elevation. Three CapaS values are determined for each basin representing the "modern" lake extent. The current lake extent is dependent on human modification of the basin and is therefore represented by a historic lakeshore elevation in CapaS computations.

The three CapaS values for the Lake Clover and Franklin valleys represent maximum, moderate, and minimum "modern" lake extents, based on pre-diversion lakeshore elevations. These CapaS values are then used as inputs for modeling the paleo-lake, allowing for variation in model predictions. Inputs for temperature in the paleo-lake calculation are slightly different from the previously described modern modeling inputs. Temperature grid inputs are representative of four temperature variants: 0° (identical to modern conditions), -3.0°, -6.0°, and -9.0°C. The model also accounts for changes in insulation from the construction of the shoreline to the present; this is based upon numerical computations of insolation from Laskar et al. (2004). The model computes the value by which modern precipitation values would need to be multiplied to sustain the lakeshore elevation at each temperature variant. To constrain this precipitation modifier, the model is run for each of the three selected modern CapaS values. Modeling of Lake Franklin produced modern CapaS values of 95, 343, and 3700 m. Models of Snow Water Lake, the modern waterbody located in the Lake Clover basin, produced CapaS values of 140, 2400, and 7100 m. These CapaS values were used to model the three Lake Franklin and six Lake Clover shoreline elevations.

Results

The model runs result in a series of temperature and precipitation (T & Ppt) combination curves; these curves estimate suitable climate conditions for each shoreline elevation at a given CapaS value. Modeling results from the "High" and "Moderate" CapaS values for the Lake Franklin and Lake Clover basins are displayed in Figures 12 & 13; full model results including "Low" CapaS T & Ppt estimates are outlined in Tables C1 and C2.

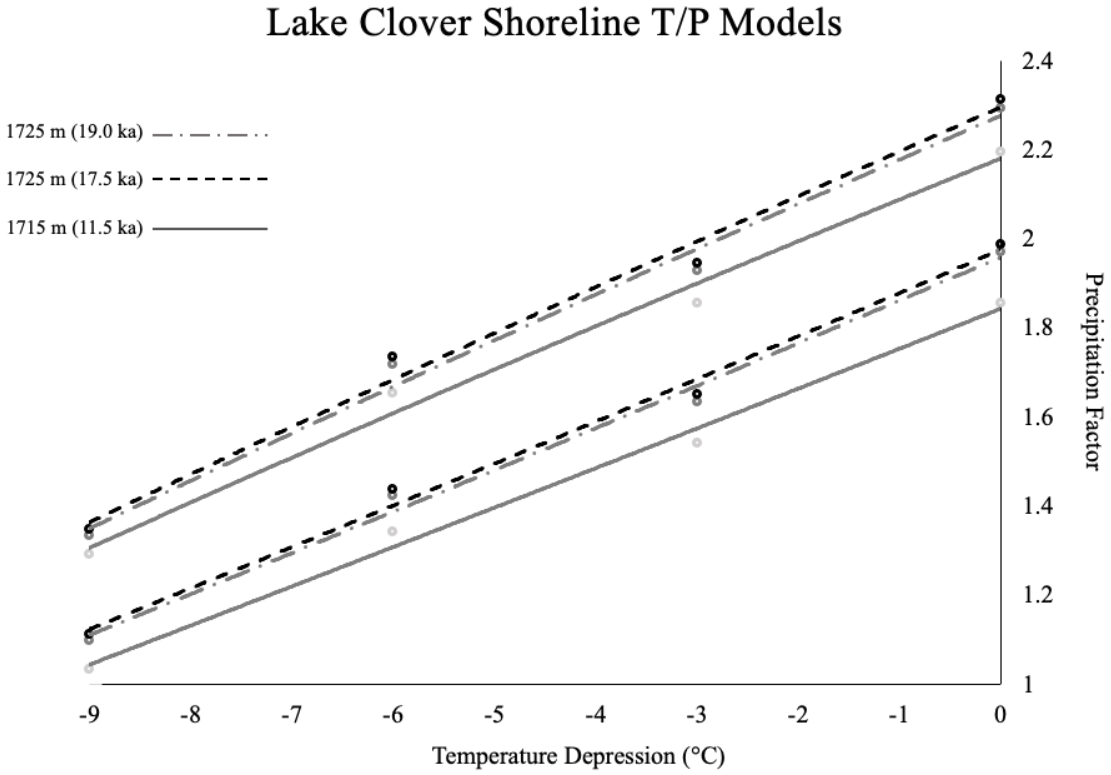

Figure 12. Temperature and precipitation curve results from water balance modeling of Lake Clover shorelines. High CapaS (7100 mm) and low CapaS (2400 mm) curves for 1725m and 1715m shorelines of Lake Clover.

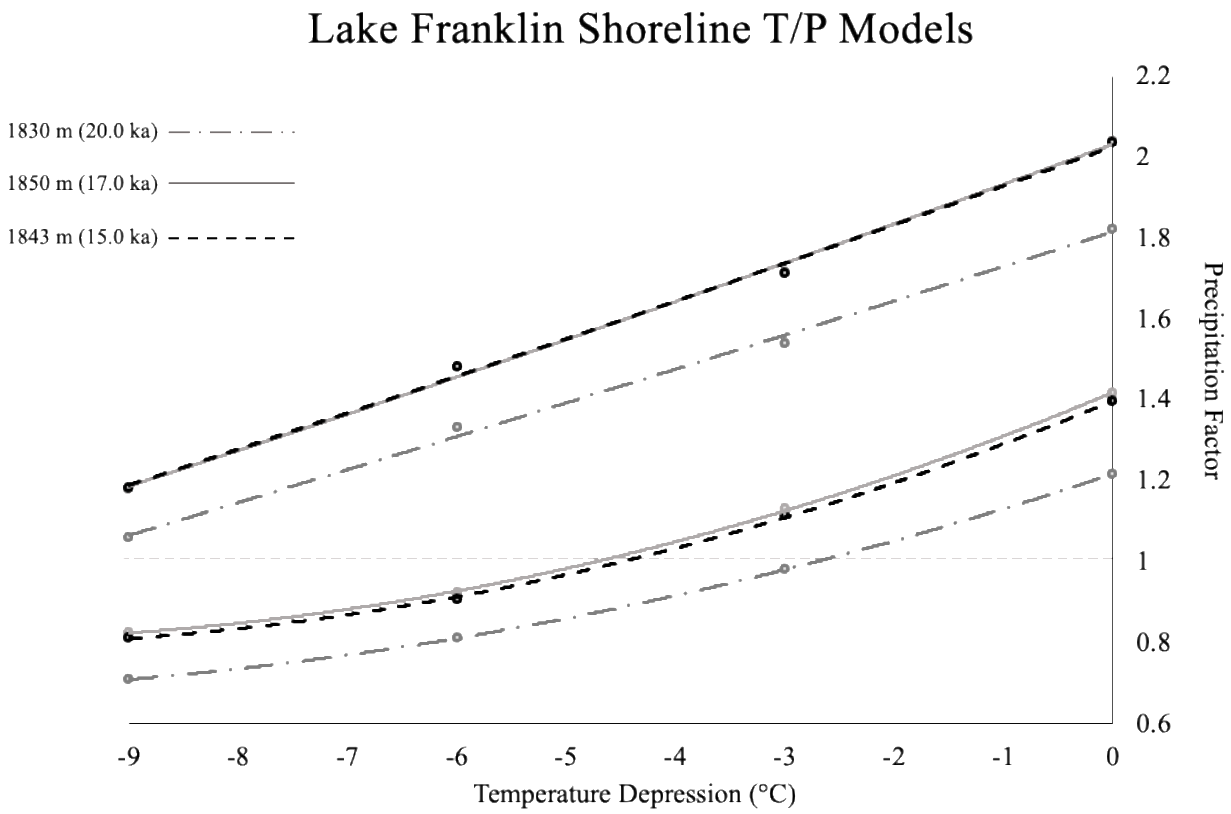

Figure 13. Temperature and precipitation (T & Ppt) curve results from water balance modeling of Lake Franklin shorelines. High CapaS (3700 mm) and low CapaS (340 mm) curves for 1830 m, 1850 m, and 1843 m shorelines of Lake Franklin.

Two T & Ppt curves from each shoreline elevation are plotted in Figures 12 and 13, one for the "High" CapaS and one for the "Moderate" CapaS. For Lake Clover, these are 7100 mm and 2400 mm, and for Lake Franklin, they are 343 mm and 3700 mm. These two CapaS values provide an array of potential T & Ppt combinations that would be viable to sustain each lakeshore elevation. The actual T & Ppt conditions that presided during each shoreline's occupation are predicted to fall between the "High" and "Moderate" CapaS curves. The difference in CapaS values reflects the difference in soil water capacity between the two basins. The much larger CapaS for the Lake Clover basin suggests greater soil storage potential than in the Lake Franklin Basin. As shown in Figure 12, the Lake Clover models predict that for any reasonable temperature depression, there must have been an increase from modern precipitation,

as the value of 1 on the vertical axis represents modern precipitation. The Lake Clover models predict increased precipitation with all “High” CapaS values, but for “Moderate” CapaS values, increased precipitation is only predicted with temperature depressions less than approximately 2.5 to 4.5 °C. Both Lake Clover and Lake Franklin show that younger shorelines trend toward warmer and dryer, specifically shoreline elevation 1715 m for Lake Clover and 1743 m for Lake Franklin. The Shorelines of Lake Franklin were previously modeled by Fleming (2019), but model codes have since been updated to fix issues with evaporation calculation procedures; the previous model resulted in CapaS of 140 mm, and 2420 mm.

Independently the pluvial lake modeling results are important, but the comparison to a secondary source of contemporaneous paleoclimate data is necessary to make any climate inferences based on them we need to compare to a secondary source of contemporaneous paleoclimate data. It is an accepted practice to compare the T & Ppt results from pluvial lake modeling to T & Ppt results from mass-balance glacial modeling. The results from Lake Clover and Lake Franklin were compared to glacial modeling results from within the Ruby and East Humboldt mountain ranges. Glaciers with well-constrained ages and extents have been modeled in the Overland Creek, Seitz Canyon, and Angel Lake glacial valleys (Reimers and Laabs, 2018; Truong et al., 2014; Johnson et al., 2016). Glacial model results plotted in Figure 14 follow the same general trends as the lake modeling derived T & Ppt curves. Due to the difference in slope between these glacial and lake models, regions of overlap can be identified when contemporaneous models are overlain. These regions of overlap represent approximate T & Ppt combinations at which models predict both the glacier and lake would be supported.

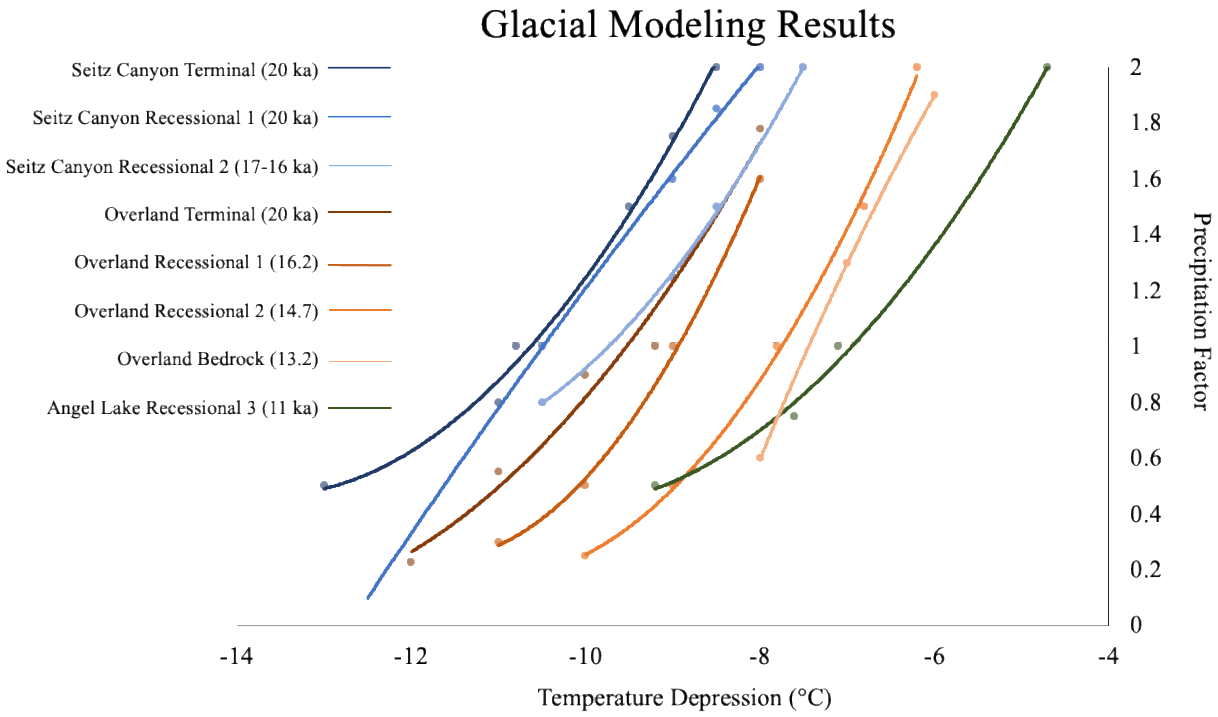

Figure 14. Temperature and precipitation curves for mass balance glacial modeling of the Seitz Canyon (Reimers and Laabs, 2018), Overland Creek (Truong et al., 2014), and Angel Lake (Johnson et al., 2016) glaciers. These glaciers were located in alpine valleys of the Ruby and East Humboldt ranges.

Due to the widespread in ages of modeled Lake Clover and Lake Franklin shorelines and the more limited spread in ages of available glacial models, results have been grouped into three age intervals. During the interval 20-19 ka (Figure 15), the Lake Franklin shoreline at 1830 m and the Lake Clover shoreline at 1725 m were plotted against glacial models from Overland Creek and Seitz Canyon. Specifically terminal moraines from Seitz Canyon and Overland Creek and a recessional moraine from Seitz Canyon. The region of overlap in model predictions suggests that a combination of approximately modern precipitation levels and a temperature depression of between 10 to 12 °C likely occurred within the 20-19 ka interval.

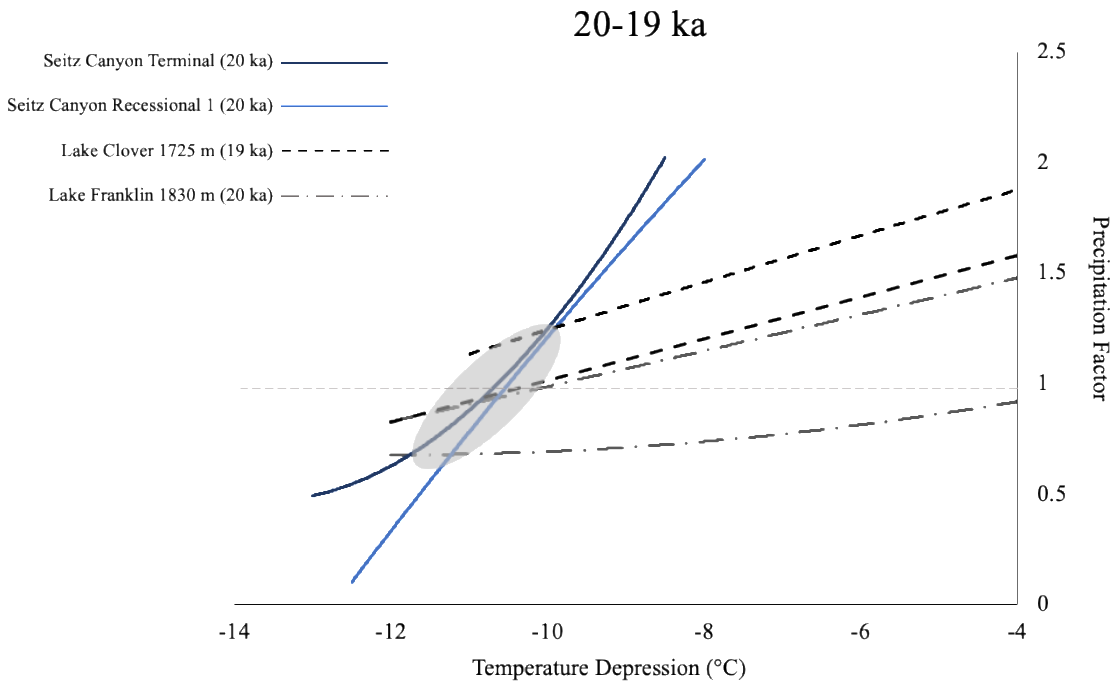

Figure 15. Temperature and precipitation curves from Lake Clover (1725 m), Lake Franklin (1830 m), and Seitz Canyon (Terminal and Recessional 1), which fall within the 20-19 ka interval, are plotted together for comparison. The grey region indicates an area of model overlap, a reasonable prediction for climate parameters at some point during the 20-19 ka interval.

Over the interval of 17-15 ka (Figure 16), the Lake Franklin shorelines at elevation 1850m and 1843m, along with two younger Lake Clover occupations of the shoreline at 1725m, were compared to glacial modes from Overland creek and Seitz Canyon. Two recessional moraines from Overland Creek (16.2 ka and 14.7 ka) and one recessional moraine from Seitz Canyon (17-16 ka) were available within this time interval. The region of model overlap identified for the 17-15 ka interval is near or slightly above modern precipitation, with a temperature depression ranging from 7 to 10.5°C. This suggests that the 17-15 ka interval was distinctly warmer and potentially wetter than the 20-19 ka interval. Temperature and precipitation curves from Overland Creek recessional 1 (16.2 ka) and Overland Creek recessional 2 (14.7) are offset by approximately 1 °C, indicating that within this 17-15 ka interval some climatic changes likely occurred. Ideally this interval would be further subdivided,

however, at present there is not enough chronological precision available to do so with confidence.

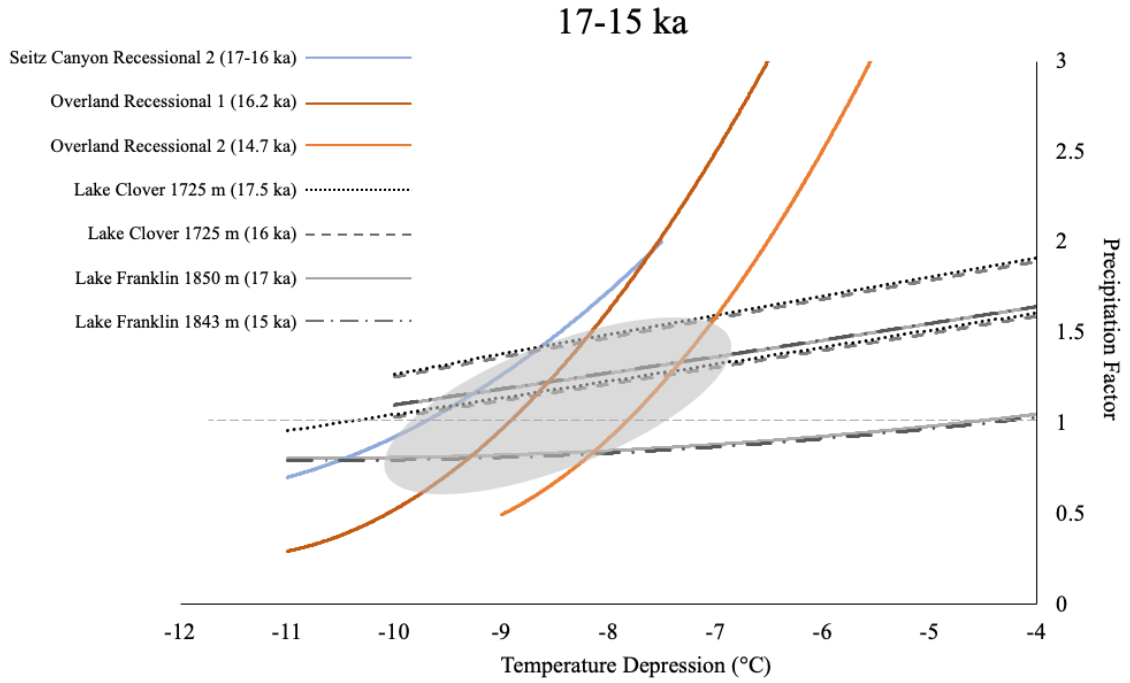

Figure 16. Temperature and precipitation curves from Lake Clover (1725 m), Lake Franklin (1850 m, 1743 m), Seitz Canyon (Recessional 2), and Overland Creek (Recessional 1 & 2), which fall within the 17-15 ka interval, are plotted together for comparison. The grey region indicates an area of model overlap, a reasonable prediction for climate parameters at some point during the 17-15 ka interval.

At 13-11 ka (Figure 17), the youngest interval compares Lake Clover shorelines at 1713m and 1715m against glacial modeling from Overland Creek and Angel Lake in the East Humboldt Mountains. The third Overland Creek model (13.2 ka), a glacially scoured bedrock exposure, and the third Angel Lake recessional moraine model (11 ka) are available for comparison with the 13-11 ka time interval. The region of overlap during the 13-11 ka interval predicts significantly higher precipitation and increased warming. The temperature depression predicted ranges from approximately 5.5 to 7.5 °C, and the precipitation factor predicted ranges from approximately 1.2 to 1.8 × modern precipitation.

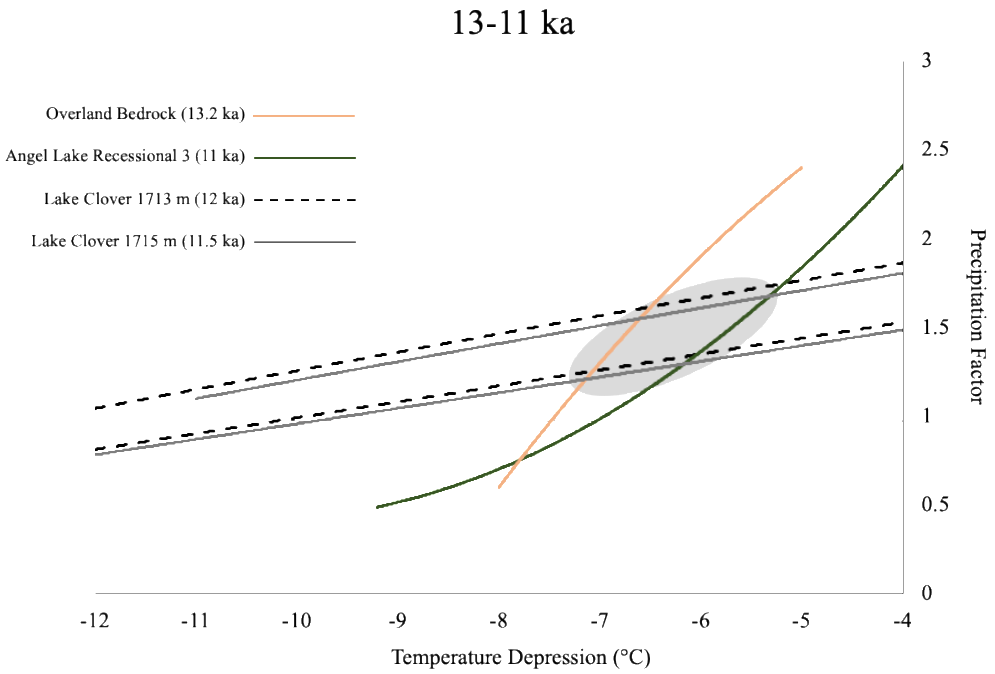

Figure 17. Temperature and precipitation curves from Lake Clover (1713 m, 1715 m), Overland Creek (Bedrock), and Angel Lake (Recessional 1), which fall within the 13-11 ka interval, are plotted together for comparison. The grey region indicates an area of model overlap, a reasonable prediction for climate parameters at some point during the 13-11 ka interval.

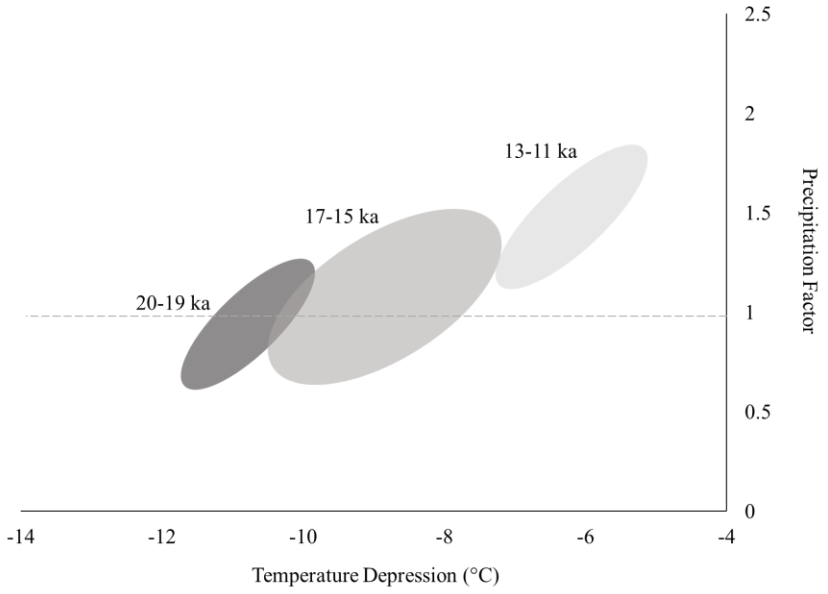

Figure 18. Regions of overlap from Figures 15, 16, and 17 are plotted together to show general trends in predicted climate parameters. Individual regions of overlap are labeled by time interval.

Discussion

Water balance modeling of Pluvial Lakes Clover and Franklin suggests that general trends over the 9 kyrs between 20 and 11 ka were towards warmer at wetter conditions (Figure 18). Taking average values for each of the intervals, we see a predicted warming by approximately 5 °C and a predicted increase in precipitation by approximately 50%. The temporal resolution of presented estimates is limited by the availability of glacial modeling, meaning that we can only approximate temperature and hydroclimate trends over these relatively large intervals with the currently available data.

Quirk et al. (2018) conducted a similar comparison between an LGM age Wasatch range glacier model (20.2 ± 1.1 ka) and a previously published T & Ppt curve from Lake Manly in Death Valley (22.5-20 ka) (Matsubara and Howard, 2009). This comparison resulted in a probable T & Ppt range of -10 to -7.9 °C and 0.8 to 1.4 × modern precipitation (Quirk et al., 2018). The prediction from Quirk et al. (2018) falls both warmer and wetter than predictions from Lake Franklin and Clover models of the same age, aligning more closely with the T & Ppt's predicted for 17-15 ka. Quirk et al. (2018) acknowledged that the distance between the Wasatch Range and Lake Manly in Death Valley might affect the results as there was likely climatic variability across the southwestern U.S.

Ibarra et al. (2014) calculated precipitation changes between the LGM and the post-LGM highstands of Lake Surprise, located on the Nevada/California border in northwestern Nevada, through isotope mass balance modeling. Results indicated that during the LGM, there was an increase in precipitation by 2.5 to 18.2% and a reduction in lake surface evaporation by approximately 36% relative to modern (Ibarra et al. 2014). Results from the 17-15 ka interval, which contains the Lake Surprise regional pluvial maximum, suggested an increase in

precipitation by approximately 75% relative to modern (Ibarra et al., 2014). Model-based estimates from Pluvial Lakes Franklin and Clover also suggest increasing precipitation from the LGM to 17-15 ka, but not to the degree that the Lake Surprise model has predicted.

Kirby et al. (2018) studied sediments collected from Lake Elsinore in coastal southern California to assess the Pacific southwest's hydroclimate over the interval 32-10 ka. Results suggest that the local LGM (23. 3 ka) was dominated by a cooler and wetter climate relative to modern (Kirby et al., 2018). The subsequent interval (19.7-14.4 ka) showed trends toward warmer and wetter conditions, peaking at 14.4 ka (Kirby et al., 2018). Results also show that the following interval (14.4-10.1 ka) experienced a general trend of climatic warming and reduction in precipitation, interrupted by a short period of wetter conditions (13-12.4 ka) (Kirby et al., 2018). Trends observed by Kirby et al. (2018) are broadly consistent with model-based climate estimates for Lakes Clover and Franklin. Results from the 13-11 ka interval do not suggest a climatic drying but could be related to a brief return to wet conditions consistent with the 13-12.4 ka interval identified by Kirby et al. (2018).

Conclusion

Model-based temperature and precipitation estimations presented here for the Lake Clover and Lake Franklin basins are consistent with paleoclimate records from the southwestern U.S. (Lachniet et al., 2011; Ibarra et al., 2014; Oster et al., 2015; Kirby et al., 2018; Lora and Ibarra, 2019). These records all suggest trends toward climatic warming and indicate periods of significantly enhanced effective moisture during the last deglaciation. Climate modeling results from Lora and Ibarra (2019) indicate an approximately 5 degree C warming from the LGM to the Holocene, agreeing with the degree of warming estimated by the water balance modeling of Pluvial Lakes Franklin and Clover. Several studies attribute the evident increase in effective

moisture to a southward deflection of the Polar Jet Stream caused by advances of the Laurentide and Cordilleran ice sheets (Ibarra et al., 2014; Oster et al., 2015; Hudson et al., 2019; Lora and Ibarra, 2019). Results from Lora and Ibarra (2019) also indicate an abrupt reduction in winter precipitation delivery to the southwestern U.S. beginning 15 kya, resulting from an enhanced Aleutian Low and a shift to southwesterly moisture delivery. Decreases in mean annual P – E during the Bølling-Allerød result from a simultaneous increase in evaporation and transition to more transient precipitation (Lora and Ibarra, 2019). The increase in precipitation predicted within the 13-11 ka interval is inconsistent with transient climate modeling (Lora and Ibarra, 2019) and speleothem records (Lachniet et al., 2020), but may align with the wet period (13~12.4 ka) observed by Kirby et al. (2018).

CHAPTER 4: UAS SURVEYING OF THE WHEELER PEAK ROCK GLACIER

Introduction

Understanding rock glacier behavior has historically been lacking due to the complexity of effective measurement at an appropriate time scale. However, recognizing their existence and potential hydrologic importance is key to forecasting how high alpine ecosystems will respond to climatic shifts. Generally, responses to changes in climate conditions are delayed for debris insolated ice-bodies, and long-term monitoring aims to detect minute changes over extended periods. There is interest in the capacity for UAS-based repeat photogrammetry of these features to detect motion and volumetric change (Bliakharskii et al., 2019; Lewińska et al., 2021), but the first step in that process is to understand the limitations and advantages of this type of surveying in the challenging environment of a high-altitude glacial cirque.

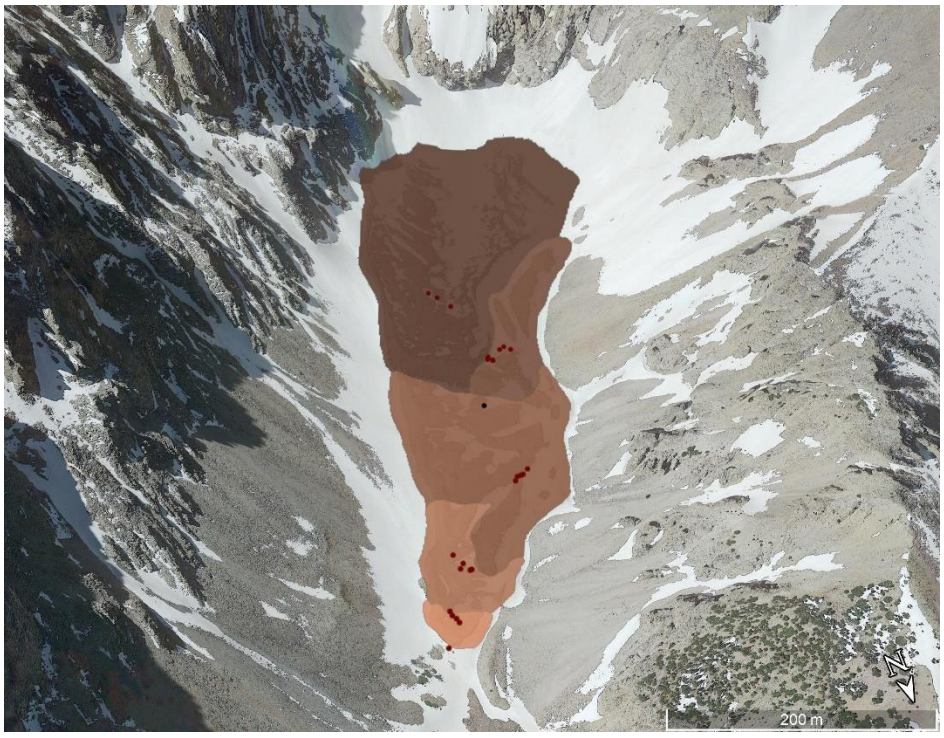

Figure 19. Topographic map of Wheeler Peak rock glacier with lobes highlighted by polygons graded from tan to brown. Red points mark boulders used in total station surveying, and the black point marks the take-off location for UAS flights. Satellite imagery obtained from Google Earth.

The Wheeler Peak rock glacier is situated within a north-facing cirque below Wheeler Peak and is composed of several lobate block fields (Figure 19). The rock glacier's lobes can be easily identified by their steep frontal slopes exposing the coarse blocks that make up the surface and finer-grained sediments, which are representative of the material in the rock glacier's core. If the ice-containing core of the rock glacier, which enables slow down-valley flow, is thinning, then we would expect to observe a decreased rate of motion or stagnation of the previously active upper lobes.

Day et al. (2018) reported total station survey results for the Wheeler Peak rock glacier; over the last nine years, total station surveying has identified motion in the down valley direction at a rate of approximately 20-40 centimeters per year across the upper lobes, while the lower lobes near the snout of the rock glacier have remained stagnant. Motion within the upper portion of the rock glacier implies the existence of interstitial or buried ice capable of supporting slow movement of the lobes. The presence of perennial ice within the core of the rock glacier is also evidenced by persistent winter temperature readings of less than -5°C at the base of the insulating snowpack, suggesting the existence of permafrost near the surface of the rock glacier.

The lower portion of the rock glacier is much steeper and features many small deformation ridges. The upper portion of the glacier is situated at the head of the cirque and is a relatively level plane separated from the lower portion by a substantial deformation ridge. Monnier et al. (2011) attributed a similar feature on the Thabor rock glacier in the Northern French Alps to compressive thrusting, consistent with the previously mentioned differential rate of motion between upper and lower regions of the rock glacier.

Methods

UAS imagery of the Wheeler Peak rock glacier has been collected over the course of two field seasons, the late summer of both 2018 and 2019. This is the optimal season for finding long periods of suitable weather conditions for UAS flights while also having a low likelihood of snowpack present on the glacier's surface. When determining if weather conditions are safe for flying precipitation, cloud cover, wind speed and direction, and humidity must be considered (Tmušić et al., 2020).

Permits for UAS surveying within GBNP were obtained through the national park offices for each field season. Generally, human traffic is limited on the surface of the rock glacier, but as it is a significant attraction for park patrons, a member of the group must be placed on the trail near the nose of the rock glacier to communicate with hikers and act as a line-of-sight observer during UAS flights. The UAS pilot and ground observers must maintain a clear line of sight with the drone and relay information back to the pilot concerning proximity to cirque walls. The UAS used in the Wheeler Peak surveys is an off-the-shelf DJI Inspire 1 equipped with a Zenmuse X3 camera. Flight time per battery is limited to approximately 15 minutes due to cooler air temperatures and low atmospheric pressure at high altitudes. Upper and lower portions of the rock glacier are surveyed independently due to line-of-sight restrictions. In order to create an appropriately georeferenced surface model through structure-from-motion photogrammetry, ground control points were placed, and positions were recorded with high precision GNSS. Ground control points used in both 2018 and 2019 were color-blocked one-foot square tiles. These tiles were spread across the rock glacier, distributed as evenly as possible on the rocky terrain, and positions were recorded with a handheld Trimble GNSS (Global Navigation Satellite System) receiver.

During the 2018 field season, weather conditions limited the survey's extent and quality, resulting in nearly full coverage of the lower but only partial coverage of the upper portion of the rock glacier. The flight paths for these surveys were manually controlled by Dr. Benjamin Laabs and flown at a stable elevation of approximately 3425m, or 30 m above the take-off point (Figure 19).

Three flights were conducted during the 2019 field season over the lower portion of the rock glacier, two vertical angle flights, and one oblique (60 degree) angle flight. Including oblique imagery improves the capture of inclined and depressed surfaces (Manfreda et al., 2018), which are abundantly present on the rock glacier. The flights were guided by a planned flight path created with the Map Pilot application and were flown at a stable elevation of approximately 3387m, or 50m above the take-off point. Sixteen ground control points were placed for flights over the lower portion of the rock glacier and remained in the same position for all three flights. Unfortunately, during the first flight over the upper portion of the rock glacier, the UAS lost GPS connection and was damaged, preventing further surveying during the 2019 field season.

A third field season, which would have been focused on the coverage of the upper portion of the rock glacier, was planned for the summer of 2020, but due to travel restrictions related to the global pandemic, no further surveys were able to be conducted. However, sufficient imagery was captured over the 2018-19 field seasons to analyze the reproducibility of models produced through structure-from-motion algorithms based on the aerial imagery. Digital surface models for the rock glacier were created for six image sets: 18V - 2018 Vertical, $19V_1$ - 2019 Vertical 1, $19V_2$ - 2019 Vertical 2, 19O - 2019 Oblique, $19V_1O$ - 2019 Vertical 1 + Oblique, and $19V_2O$ - 2019 Vertical 2 + Oblique.

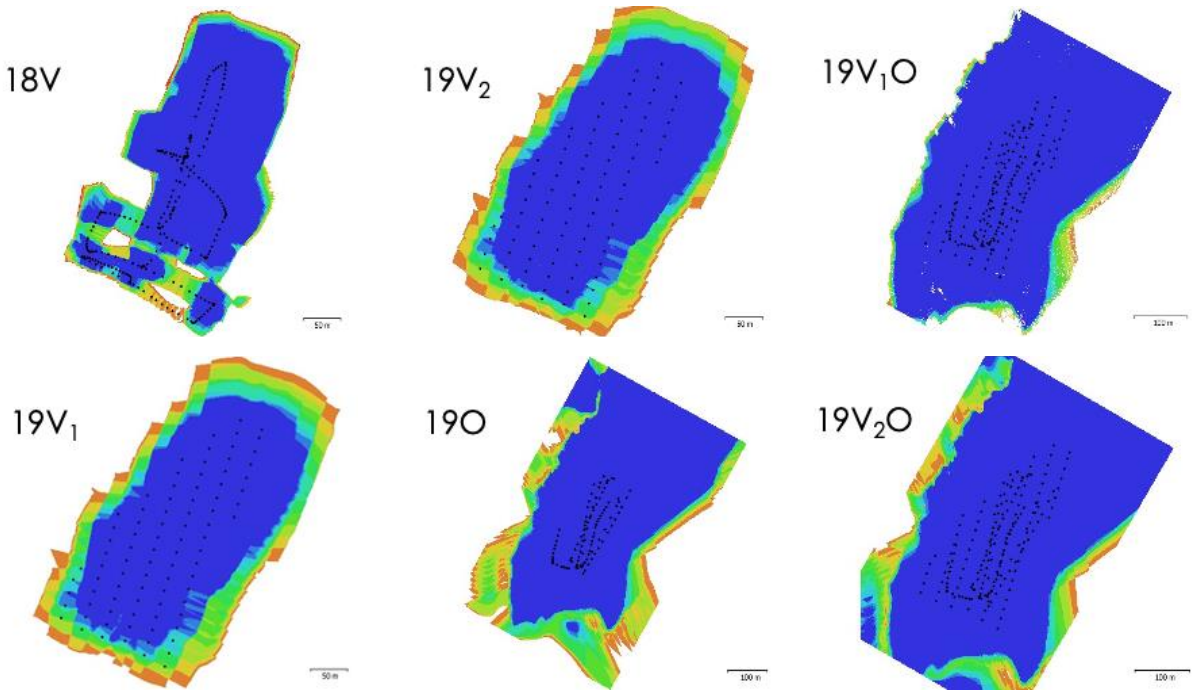

Figure 20. Image overlap maps for the six image sets modeled in Agisoft Metashape: 18V (2018 Vertical), $19V_1$ (2019 Vertical 1), $19V_2$ (2019 Vertical 2), 19O (2019 Oblique), $19V_1O$ (2019 Vertical 1 + Oblique), and $19V_2O$ (2019 Vertical 2 + Oblique). The number of overlapping images scaled from blue (≥ 9 overlapping images) to red (1 image).

Each image set was processed through the Agisoft Metashape Professional (AMP) program to generate digital elevation models DEMs for each survey flight. When images are loaded into AMP, the program aligns the photos, creating tie-points and generating a sparse point cloud. Processing specifications and inputs are provided in Table D1. Any photos that could not be automatically aligned can be manually aligned by assigning tie-pints to overlapping images. Control point GNSS location can be imported into AMP from a CSV file and should include X, Y, and Z locations along with vertical and horizontal errors. Each control point is displayed in its approximate position on the images that AMP has predicted the point was captured. The user then reviews the images and connects the control points to their appropriate positions on the images. AMP realigns the photos based on these manual connections to the control points, minimizing control point alignment error. It is important to note that for the 2018 flight,

positional information for ground control points was of insufficient resolution, so the ground surface created from the 2018 flight uses positional information from the 2019 ground control points connected to their approximate image positions. We have justified the use of these ground control points based on previous surveys, which show that the lower portion of the rock glacier remains relatively static. The 2019 ground control points were generally placed in the same positions as the 2018 ground control points, as there are limited flat surfaces for tile placement across the rock glacier surface.

At this point, AMP is used to create a dense point cloud generated by pairwise computation based on image depth maps. A mesh surface is computed for the dense point cloud and may now be texturized. Each project processed through AMP was exported as an LAS file, a binary format for storing point cloud data. LAS files for each project were then imported into ArcGIS Pro (ArcGIS) to be converted into DEMs. The DEM resolution was set to 0.5 m, reflecting the average GNSS uncertainty of ground control point locations. DEMs were subtracted from one another in a pairwise fashion to assess variation in the ground surface models produced by the six image sets; the outputs of these DEM subtractions will be referred to as ‘difference rasters.’

Results

Dense point clouds generated in the AMP program for each image set are ultrahigh-resolution surface models of the Wheeler Peak rock glacier. The resolution of these models is impressive, but this resolution cannot be preserved for analysis purposes. The resolution of DEMs created in ArcGIS is limited to the measured GNSS uncertainty and is therefore defined as 0.5 m.

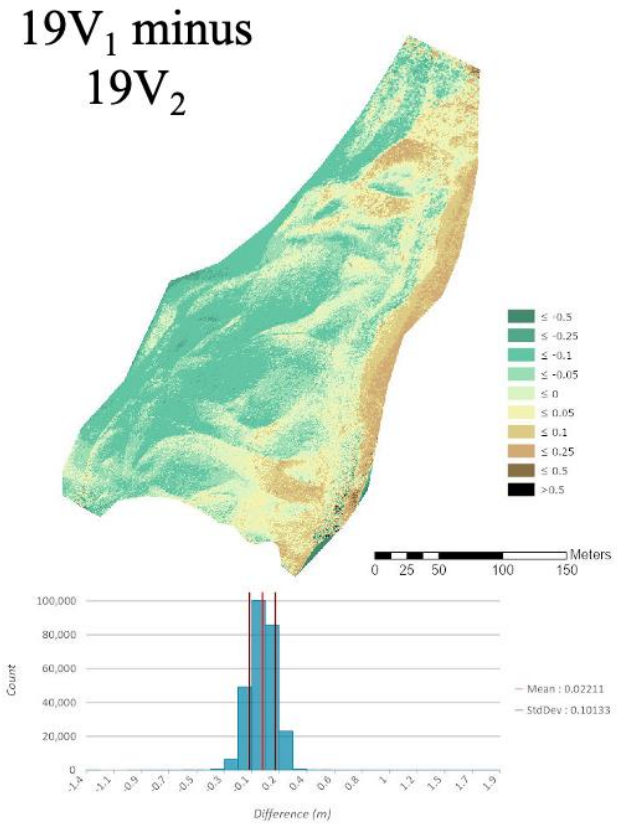

Figure 21. Difference raster comparing $19V_1$ and $19V_2$, the two vertical image sets from the 2019 field season. Difference values are depicted in map view as well as a distribution plot.

Difference rasters from the 2019 field season, shown in Figures 21 through 24, highlight areas where the second DEM of the pair has an elevation either above (shades of blue) or below (shades of brown) the first raster of the pair. As these flights were all conducted within a two-hour time frame, the difference rasters would ideally be equal to zero, but as is apparent this was not the case. What is instead observed is a highlighting of certain regions depending on the type of pairing. When the two vertical image sets ($19V_1$ minus $19V_2$, Figure 21) are compared, slopes and troughs in the rock glacier surface are highlighted as the largest areas of difference. This is not an unexpected pattern, as sloping surfaces are challenging to capture with vertical imagery alone.

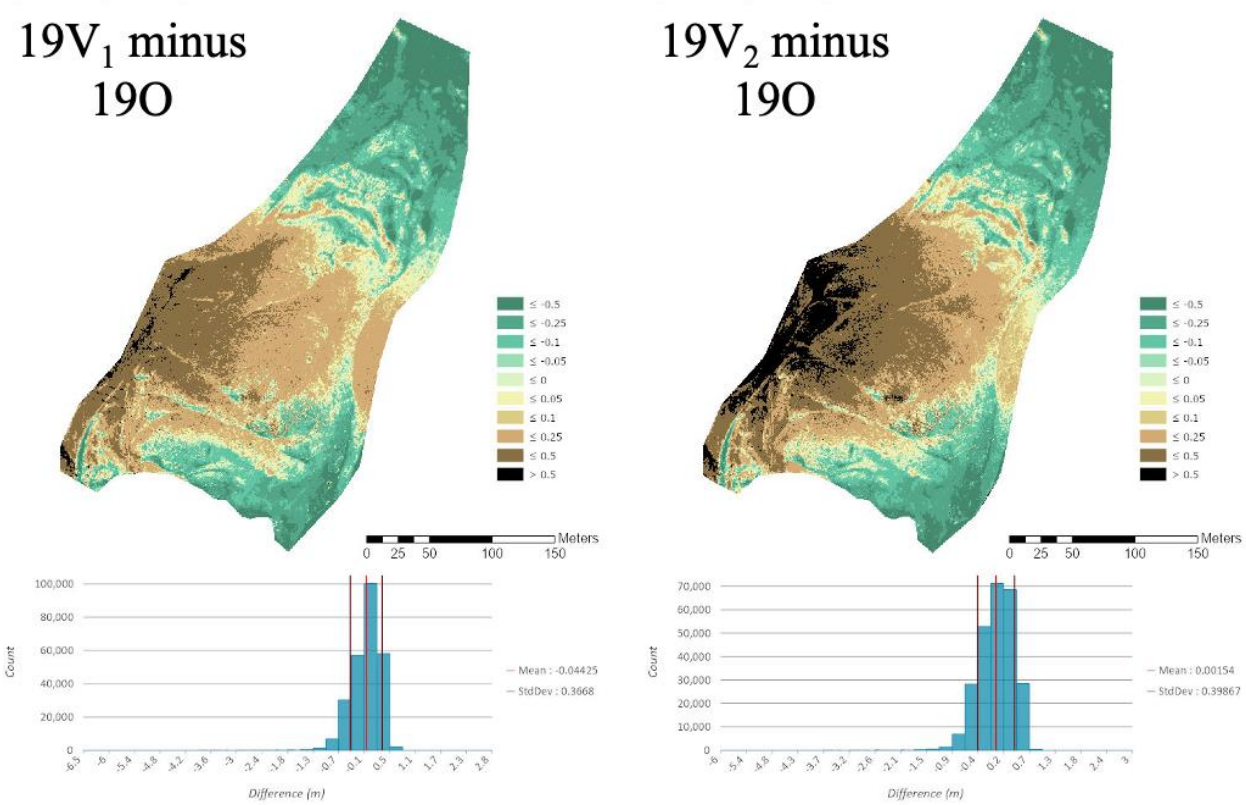

Figure 22. Difference rasters comparing $19V_1$ & 19O, and $19V_2$ & 19O; the two vertical image sets against the oblique image set from the 2019 field season. Difference values are depicted in map view as well as a distribution plot.

When a vertical and an oblique image set ($19V_1$ minus 19O, or $19V_2$ minus 19O; Figure 22) are compared, the resulting difference raster shows what appears to be a systematic radial error. James and Robson (2014) attribute this 'doming' to structure-from-motion DEMs built with parallel camera angles and lacking sufficient control points. The inclusion of oblique camera angle images is suggested as a partial solution to this problem (James and Robinson, 2014). This same effect is observed to a lesser extent when comparisons contain a vertical image set and a vertical + oblique image set ($19V_1$ minus $19V_1O$, $19V_2$ minus $19V_1O$, $19V_1$ minus $19V_2O$, or $19V_2$ minus $19V_2O$; Figure 23).

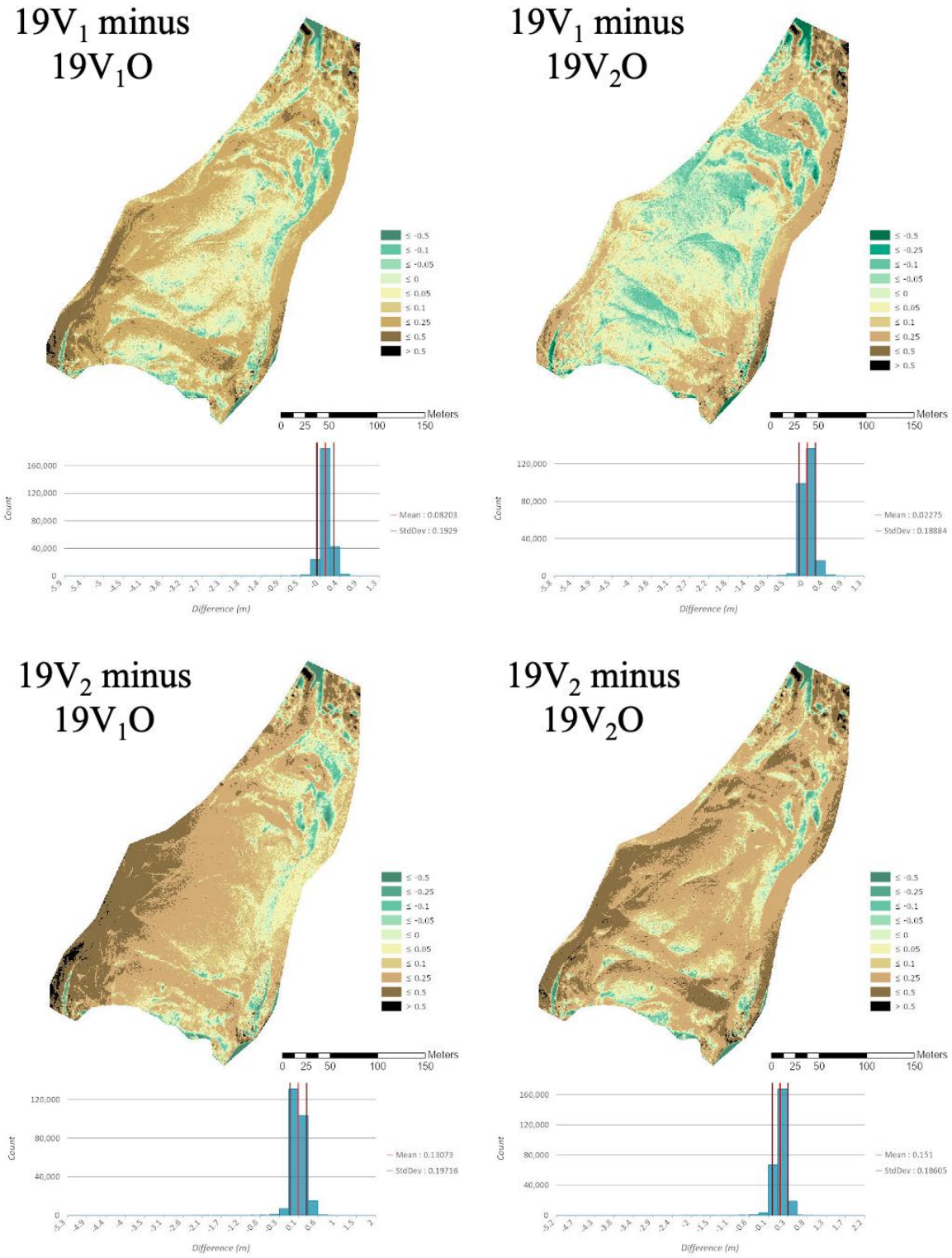

Figure 23. Difference rasters comparing $19V_1$ & $19V_1O$, $19V_2$ & $19V_1O$, $19V_1$ & $19V_2O$, and $19V_2$ & $19V_2O$; the two vertical image sets against the vertical & oblique combination image set from the 2019 field season. Difference values are depicted in map view as well as a distribution plot.

The comparison with the smallest standard deviation is $19V_1O$ minus $19V_2O$ (2019 Vertical 1 + Oblique minus 2019 Vertical 2 + Oblique, Figure 24). Like $19V_1$ minus $19V_2$, this difference raster highlights slopes and troughs within the rock glacier and shows no sign of the systematic radial error observed previously.

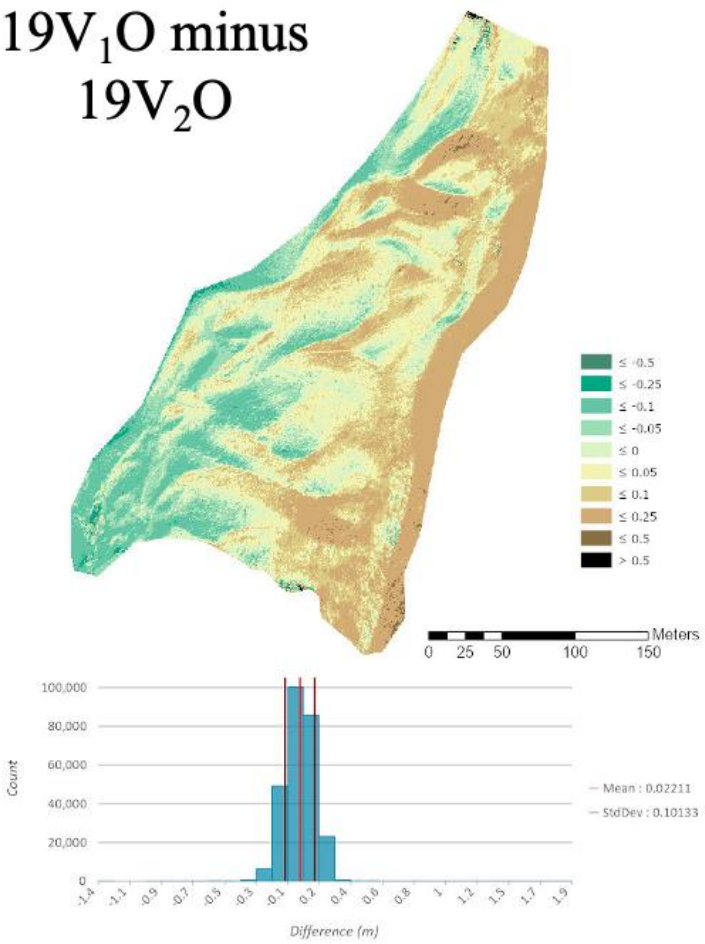

Figure 24. Difference raster comparing $19V_1O$ & $19V_2O$, the two vertical & oblique image sets from the 2019 field season. Difference values are depicted in map view as well as a distribution plot.

We appear to see a different type of systematic error in the $19V_1$ minus 18V and $19V_2$ minus 18V difference rasters, where one surface model is oblique to the other. This lateral systematic error is likely due to the lack of ground control in the 2018 model. General trends show 18V at a higher elevation than $19V_1$ and $19V_2$ on the eastern edge and a lower elevation

than $19V_1$ and $19V_2$ on the western edge (Figure 25). There are also regions on either side of the rock glacier where 18V falls far below $19V_1$ or $19V_2$. These regions appear to be partially related to snowpack, which was not present in 2018 but was present in 2019.

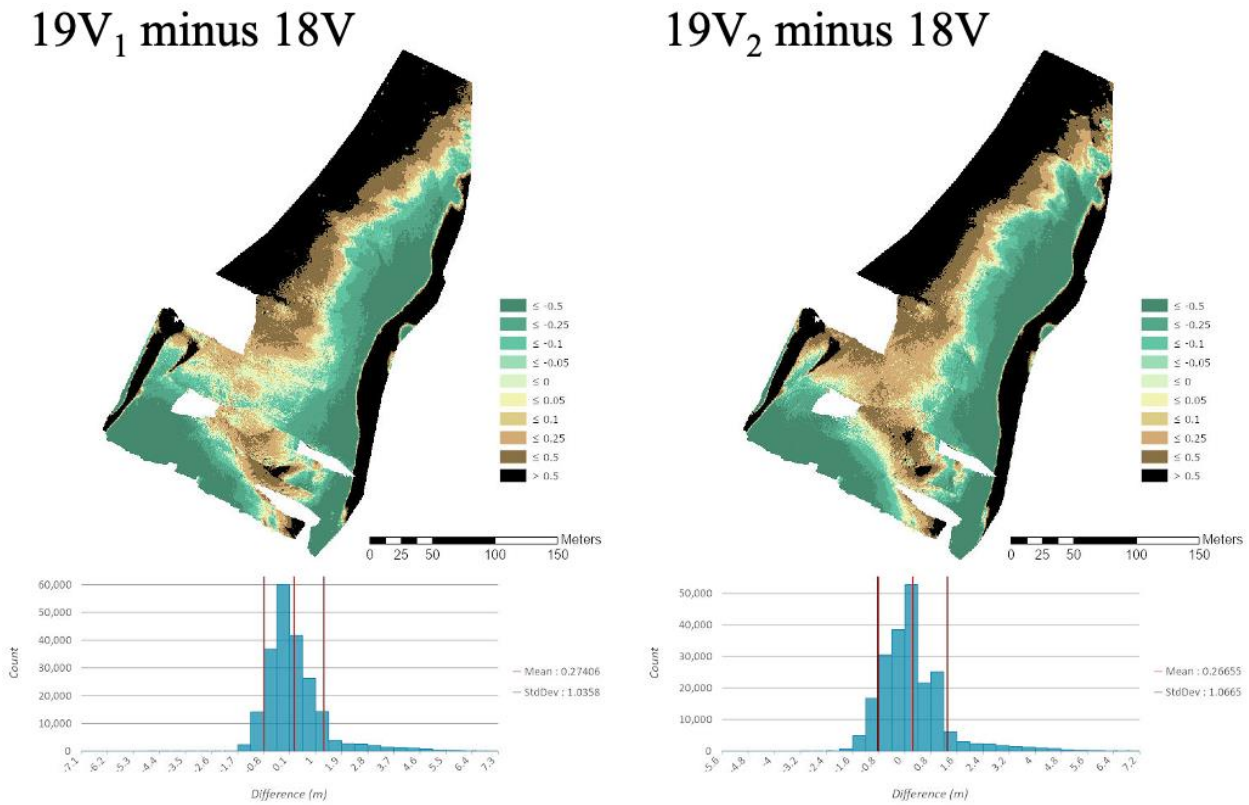

Figure 25. Difference rasters comparing $19V_1$ & 18V, and $19V_2$ & 18V; the two vertical image sets from the 2019 field season against the vertical image set from the 2018 field season. Difference values are depicted in map view as well as a distribution plot.

Discussion

This analysis aims to determine the steps this research group can take to collect the most useful data in the most efficient way. Three significant issues must be addressed: maximizing GNSS precision, effectively capturing surface topography, and minimizing the risk of systematic errors. These three issues can be targeted through specific changes to flight procedures.

With current technology, the resolution-limiting factor is GNSS uncertainty, and receiving a signal from a sufficient number of satellites in a confined valley is difficult. The platform UAVforecast^{TM} provides forecasting for geomagnetic disruptions that may impact

satellite signal reception; this is key for ensuring both adequate measurement capacity and UAS safety (Tmušić et al., 2020). Though the uncertainty in ground control point positioning is of the utmost importance for producing a meaningful digital surface model, of even more importance is satellite reception for the UAS. A loss of satellite connection with the UAS can lead to hazardous and costly situations, and the ability to foresee geomagnetic disruptions that might put your team and equipment in danger is extremely valuable. Through the use of UAVforecast™ and other similar tools, we hope to improve the safety and quality of work in future field seasons. However, it is possible that due to site limitations, a steep-walled valley with rough surface terrain, the resolution is limited to approximately 0.5 m. If this is the case, it would be the recommendation of this study to conduct repeat surveying less frequently, improving the likelihood of capturing meaningful rock glacier change.

Further surveying of the Wheeler Peak rock glacier will collect both vertical and oblique imagery over the entire rock glacier surface, allowing for more effective analysis of surface motion and potentially volumetric change. As discussed in the methods, including oblique imagery improves the capture of inclined and depressed surfaces (Manfreda et al., 2018). Though it may be possible to use new vertical image sets to make use of previously collected vertical imagery, the recommendation based on the current body of knowledge is that the inclusion of oblique imagery, especially in areas with complex terrain, is necessary to generate an accurate digital surface model (James and Robson, 2014; Tmušić et al., 2020; Manfreda et al. 2018). What is shown in the presented rock glacier flight analysis is that mean and standard deviation are minimized when comparing vertical + oblique image combinations with one another rather than with solely vertical image sets. The $19V_1O$ minus $19V_2O$ difference raster highlighted

regions of slopes and depressions on the rock glacier surface, which are known to be the most difficult surfaces to model accurately.

When comparing vertical image sets to oblique image sets, the doming effect is a systematic error present when models are built with solely vertical imagery. The doming is not clearly visible in the 18V, $19V_1$, and $19V_2$ digital surface models but may be more evident in models of surfaces with less pronounced relief. The natural shape of the surface appears to mask the systematic error present in the models. When 19O is subtracted from $19V_1$ or $19V_2$, this systematic error becomes striking, highlighting the importance of capturing the surface from multiple camera angles. Based on the $19V_1$ minus $19V_2$ difference raster, it appears that when two models are both developed from solely vertical image sets, they may be able to be compared to one another even though they possess this systematic error. With the knowledge that the conclusions from such comparisons may be less reliable, this method may still allow for comparison to previously captured vertical angle imagery. In the case of the 2018 survey imagery, comparisons with the 2019 imagery may have been possible if appropriate georeferencing information was available for both field seasons. It is recommended to capture a combination of vertical and oblique imagery with sufficient ground control point coverage. Resolution may also be improved through additional ground control points with a more uniform distribution across the rock glacier surface. Manfreda et al. (2018) found that the distribution and number of control points have the most considerable impact on the accuracy of the resulting products. Though, the rock glacier surface is not conducive to truly uniform ground control point distribution, as steep slopes both on the rock glacier and alongside the rock glacier restrict potential control point locations.

Conclusion

The record of repeat UAS-based photogrammetry developed through continued surveying will allow for the identification of internal regions of compression or dilation within various lobes of the rock glacier, and therefore an approximation of ice-core thickness. Improvements to methodology in future surveys including increased control point coverage, inclusion of oblique angle photography, and the employment of tools such as UAVforecast™ aim improve the resolution from the present 0.5 meters. Further, improved understanding of the rock glacier's mechanics will allow for future assessment of the potential contributions to streamflow in Lehman Creek, yielding data that can be used to inform water resource management decisions within Great Basin National Park. Enhancing the ability to quantify motion and volumetric change of rock glaciers will also allow for a broader assessment of the health of perennial-ice containing features throughout the Great Basin.

CHAPTER 5: CONCLUSION

Studying the impacts of climate change, both past, and present, on features such as glaciers and pluvial lakes provides vital context for the assessment of glacial stability and longevity. Furthermore, contextualizing hydrologic and environmental changes that have accompanied past glacial retreats improves our ability to respond to modern climate change.

Cosmogenic ^{10}Be exposure ages for the Baker Creek valley moraines within Great Basin National Park provide limits to the timing of the LGM maximum glacial extent as well as the apparent pause in glacial retreat associated with the construction of the up-valley moraine. The Baker Creek valley glacier was among the two largest glaciers in the South Snake Range during the last Pleistocene glaciation, occupying a primary drainage of Baker Peak (Osborn and Bevis, 2001). The terminal moraine has an average exposure age of 21.0 ± 0.6 ka, coinciding with the global expansion of glaciers and ice sheets to their maximum extents due to decreases in northern hemisphere summer insolation, tropical Pacific sea surface temperatures, and atmospheric CO_2 (Clark et al., 2009). The recessional moraine has an average sample age of 14.0 ± 1.0 ka and agrees with the up-valley recessionals from the Wasatch and Santa Rosa ranges (Quirk et al., 2018; Fleming et al., 2019). The presence of the Baker Creek glacier at approximately 50% of its LGM extent until 14 ka suggests that some high mountain glaciers persisted until after the beginning of Bølling-Allerød and even until Lake Bonneville began to fall. The Bølling-Allerød interstadial, the period in which the Baker Creek recessional moraine was constructed, is noted for warmer and drier conditions related to an enhanced Aleutian Low and northward deflection of the Pacific winter storm track (Otto-Bliesner et al., 2006; Oster et al. 2015; Lora and Ibarra, 2019). The continued expansion of glacial chronologies during the late stages of retreat would further limit the presence of glaciers in the Great Basin. Currently, the

disappearance of glaciers from the Great Basin landscape is not well constrained, but this interval may be elucidated through continued dating of available up-valley moraines.

Modeling late Pleistocene Pluvial Lakes Franklin and Clover expands the available climate chronology for the Great Basin region. Pluvial lakes are unique, expansive features that had a substantial impact on the environment of the Great Basin. Shoreline ridges are constructed by these pluvial lakes when lake levels remain stable and dating these ridges allows researchers to build lake-level chronologies. Late Pleistocene Lakes Clover and Franklin are situated adjacent to the Ruby and East Humboldt ranges, allowing for direct comparison and approximation of the climate conditions which would support contemporaneous glacial moraine deposition and shoreline ridge construction. Presented temperature and precipitation approximations predict that over the interval of 20-11 ka, the region experienced warming by approximately 5 °C and an increase in precipitation by approximately 50%. Enhanced effective moisture during the pluvial highstand has been attributed to increased delivery of winter precipitation due to southward deflection of the westerly storm track and teleconnections between conditions in the North Atlantic and winter precipitation in the southwestern U.S. (Oster et al., 2018; Hudson et al., 2019). Model-based temperature and precipitation predictions are dependent on data from previously published studies and are limited by the temporal resolution of available glacial modeling. The expansion of available glacial chronologies and models could improve the predictive ability of these models in the future. Specifically, the interval of 17-15 ka, which resulted in a broader range of temperature and precipitation predictions, should be a target for future modeling as many pluvial lakes expanded to their highstands during this interval. Expansion of up-valley moraine chronology, as mentioned above, would also improve the ability to conduct similar glacial and pluvial lake model comparisons throughout the Great Basin.

Rock glaciers are unique features, especially in environments such as the arid mountains of Nevada. The recognition of the potential hydrologic importance of rock glaciers is key to forecasting how high alpine ecosystems will respond to climatic shifts. The ability to efficiently and cost-effectively survey rock glacier features through UAS-based repeat photogrammetry would significantly improve our understanding. Previous total station surveying of the Wheeler Peak rock glacier in Great Basin National Park has identified motion in the down valley direction at a rate of approximately 20-40 centimeters per year across the upper lobes, while the lower lobes near the snout of the rock glacier are have remained stagnant (Day et al. (2015). UAS-based aerial surveying has resulted in digital surface models of the rock glacier with a resolution of 0.5 m, too coarse to detect meaningful change on an annual basis. Improvements in control point coverage, the inclusion of oblique angle photography, and the employment of tools such as UAVforecast™ may improve the resolution of produced digital surface models for future field seasons. UAS-based photogrammetry methodology discussed here can also be applied to the numerous rock glacier features identified by Millar and Westfall (2019), the stability and hydrologic importance of which are essential to assess in the modern, rapidly changing climate. Comprehensive records developed through repeat UAS-based photogrammetry allow for more efficient and cost-effective analysis of rock glacier mechanics and assessment of potential hydrologic contributions.

REFERENCES

Anderson, R. S., Anderson, L. S., Armstrong, W. H., Rossi, M. W., & Crump, S. E. (2018). Glaciation of alpine valleys: The glacier – debris-covered glacier – rock glacier continuum. Geomorphology, 311, 127–142. https://doi.org/10.1016/j.geomorph.2018.03.015

Applegate, P. J., Urban, N. M., Laabs, B. J. C., Keller, K., & Alley, R. B. (2010). Modeling the statistical distributions of cosmogenic exposure dates from moraines. Geoscientific Model Development, 3(1), 293–307. https://doi.org/10.5194/gmd-3-293-2010

Applegate, P. J., Urban, N. M., Keller, K., Lowell, T. V., Laabs, B. J. C., Kelly, M. A., & Alley, R. B. (2012). Improved moraine age interpretations through explicit matching of geomorphic process models to cosmogenic nuclide measurements from single landforms. Quaternary Research, 77(2), 293–304. https://doi.org/10.1016/j.yqres.2011.12.002

Asmerom, Y., Polyak, V. J., & Burns, S. J. (2010). Variable winter moisture in the southwestern United States linked to rapid glacial climate shifts. Nature Geoscience, 3(2), 114–117. https://doi.org/10.1038/ngeo754

Balco, G. (2011). Contributions and unrealized potential contributions of cosmogenic-nuclide exposure dating to glacier chronology, 1990-2010. Quaternary Science Reviews, 30(1–2), 3–27. https://doi.org/10.1016/j.quascirev.2010.11.003

Balco, G. (2020). Glacier Change and Paleoclimate Applications of Cosmogenic-Nuclide Exposure Dating. Annual Review of Earth and Planetary Sciences, 48, 21–48.

Balco, G., Stone, J. O., Lifton, N. A., & Dunai, T. J. (2008). A complete and easily accessible means of calculating surface exposure ages or erosion rates from 10Be and 26Al measurements. Quaternary Geochronology, 3, 174–195. https://doi.org/10.1016/j.quageo.2007.12.001

Blackwelder, E. (1931). Pleistocene Glaciation of the Sierra Nevada and Basin Ranges. Bulletin of the Geological Society of America, 42, 865–922.

Blard, P. H., & Farley, K. A. (2008). The influence of radiogenic 4He on cosmogenic 3He determinations in volcanic olivine and pyroxene. Earth and Planetary Science Letters, 276, 20–29. https://doi.org/10.1016/j.epsl.2008.09.003

Blard, P. H., Lavé, J., Farley, K. A., Fornari, M., Jiménez, N., & Ramirez, V. (2009). Late local glacial maximum in the Central Altiplano triggered by cold and locally-wet conditions during the paleolake Tauca episode (17-15 ka, Heinrich 1). Quaternary Science Reviews, 28(27–28), 3414–3427. https://doi.org/10.1016/j.quascirev.2009.09.025

Otto-Bliesner, B., Brady, E., Clauzet, G., Thomas, R., Levis, S., & Kathavala, Z. (2006). Last Glacial Maximum and Holocene climate in CCSM3. Climate, 19, 2526–2544.

Borchers, B., Marrero, S., Balco, G., Caffee, M., Goehring, B., Lifton, N., Nishiizumi, K., Phillips, F., Schaefer, J., & Stone, J. (2016). Geological calibration of spallation production rates in the CR

Brighenti, S., Hotaling, S., Finn, D. S., Fountain, A. G., Hayashi, M., Herbst, D., Saros, J. E., Tronstad, L. M., & Millar, C. I. (2021). Rock glaciers and related cold rocky landforms: overlooked climate refugia for mountain biodiversity. Global Change Biology, September 2020, 1–14. https://doi.org/10.1111/gcb.15510

Broecker, W., McGee, D., Adams, K., Cheng, H., Edwards, R., Oviatt, C., & Quade, J. (2009). A Great Basin-wide dry episode during the first half of the Mystery Interval? Quaternary Science Reviews, 28, 2557–2563. 10.1016/j.quascirev.2009.07.007

Broecker, W., & Putnam, A. E. (2012). How did the hydrologic cycle respond to the two-phase mystery interval? Quaternary Science Reviews, 57, 17–25. https://doi.org/10.1016/j.quascirev.2012.09.024

Clark, P. U., & Bartlein, P. J. (1995). Correlation of late Pleistocene glaciation in the western United States with North Atlantic Heinrich events. Geology, 23(6), 483–486. https://doi.org/10.1130/0091-7613(1995)023<0483:COLPGI>2.3.CO;2

Clark, P. U., Dyke, A. S., Shakun, J. D., Carlson, A. E., Clark, J., Wohlfarth, B., Mitrovica, J. X., Hostetler, S. W., & McCabe, A. M. (2009). The Last Glacial Maximum. Science, 325(5941), 710 LP – 714. https://doi.org/10.1126/science.1172873

Condom, T., Coudrain, A., Dezetter, A., Brunstein, D., Delclaux, F., & Jean-Emmanuel, S. (2004). Transient modelling of lacustrine regressions: Two case studies from the Andean Altiplano. Hydrological Processes, 18(13), 2395–2408. https://doi.org/10.1002/hyp.1470

Cross, M., McGee, D., Broecker, W. S., Quade, J., Shakun, J. D., Cheng, H., Lu, Y., & Edwards, R. L. (2015). Great Basin hydrology, paleoclimate, and connections with the North Atlantic: A speleothem stable isotope and trace element record from Lehman Caves, NV. Quaternary Science Reviews, 127, 186–198. https://doi.org/10.1016/j.quascirev.2015.06.016

Easterbrook, D. J., Gosse, J., Sherard, C., Evenson, E., & Finkel, R. (2011). Evidence for Synchronous Global Climatic Events: Cosmogenic Exposure Ages of Glaciations. In Evidence-Based Climate Science. https://doi.org/10.1016/B978-0-12-385956-3.10002-6

Fleming, K. (2019). Cosmogenic 10Be Surface Exposure Dating and Numerical Modeling of Late Pleistocence Glaciers and Lakes in Northwestern Nevada. North Dakota State University.

Gosse, J. C., Evenson, E. B., Klein, J., Lawn, B., & Middleton, R. (1995). Precise cosmogenic 10Be measurements in western North America: Support for a global Younger Dryas cooling event. Geology, 23(10), 877–880. https://doi.org/10.1130/0091-7613(1995)023<0877:PCBMIW>2.3.CO;2

Gosse, J. C., & Philips, F. M. (2001). Terrestrial in situ cosmogenic nuclides: theory and application. Quaternary Science Reviews, 20, 1475–1560.

Graham, J. P. (2014). Great Basin National Park: Geologic Resources Inventory Report. Natural Resource Report NPS/NRSS/GRD/NRR-2014/762.

Hemming, S. R. (2004). Heinrich events: Massive late Pleistocene detritus layers of the North Atlantic and their global climate imprint. Reviews of Geophysics, 42, 1–43. https://doi.org/10.1029/2003RG000128

Hudson, A. M., Hatchett, B. J., Quade, J., Boyle, D. P., Bassett, S. D., Ali, G., & De los Santos, M. G. (2019). North-south dipole in winter hydroclimate in the western United States during the last deglaciation. Scientific Reports, 9(1), 1–12. https://doi.org/10.1038/s41598-019-41197-y

Ibarra, D. E., Egger, A. E., Weaver, K. L., Harris, C. R., & Maher, K. (2014). Rise and fall of late Pleistocene pluvial lakes in response to reduced evaporation and precipitation: Evidence from Lake Surprise, California. Bulletin of the Geological Society of America, 126(11–12), 1387–1415. https://doi.org/10.1130/B31014.1

James, M. R., & Robson, S. (2014). Mitigating systematic error in topographic models derived from UAV and ground-based image networks. Earth Surface Processes and Landforms, 39(10), 1413–1420. https://doi.org/10.1002/esp.3609

Johnson, M., Laabs, B.J.C., Bradley, R.A., and Munroe, J.S., 2016. Climate change during deglaciation of the Angel Lake valley, East Humboldt Mountains, Nevada, U.S.A. Geological Society of America, Abstracts with Programs, Vol. 28, No. 2, doi:10.1130/abs/2016NE-272834.

Kirby, M. E., Heusser, L., Scholz, C., Ramezan, R., Anderson, M. A., Markle, B., Rhodes, E., Glover, K. C., Fantozzi, J., Hiner, C., Price, B., & Rangel, H. (2018). A late Wisconsin (32–10k cal a BP) history of pluvials, droughts and vegetation in the Pacific south-west United States (Lake Elsinore, CA). Journal of Quaternary Science, 33(2), 238–254. https://doi.org/10.1002/jqs.3018

Laabs, B. J. C., & Munroe, J. S. (2016). Late Pleistocene Mountain Glaciation in the Lake Bonneville Basin. In Developments in Earth Surface Processes (Vol. 20). https://doi.org/10.1016/B978-0-444-63590-7.00017-2

Laabs, B. J. C., Licciardi, J. M., Leonard, E. M., Munroe, J. S., & Marchetti, D. W. (2020). Updated cosmogenic chronologies of Pleistocene mountain glaciation in the western United States and associated paleoclimate inferences. Quaternary Science Reviews, 242, 106427. https://doi.org/10.1016/j.quascirev.2020.106427

Laabs, B. J. C., Marchetti, D. W., Munroe, J. S., Refsnider, K. A., Gosse, J. C., Lips, E. W., Becker, R. A., Mickelson, D. M., & Singer, B. S. (2011). Chronology of latest Pleistocene mountain glaciation in the western Wasatch Mountains, Utah, U.S.A. Quaternary Research, 76(2), 272–284. https://doi.org/10.1016/j.yqres.2011.06.016

Laabs, B. J. C., Munroe, J. S., Best, L. C., & Caffee, M. W. (2013). Timing of the last glaciation and subsequent deglaciation in the Ruby Mountains, Great Basin, USA. Earth and Planetary Science Letters, 361, 16–25. https://doi.org/10.1016/j.epsl.2012.11.018

Lachniet, M. S. (2016). A Speleothem Record of Great Basin Paleoclimate: The Leviathan Chronology, Nevada. In Developments in Earth Surface Processes: Lake Bonneville a Scientific Update (Vol. 20, pp. 551–569). https://doi.org/10.1016/B978-0-444-63590-7.00020-2

Lachniet, M. S., Asmerom, Y., & Polyak, V. (2011). Deglacial paleoclimate in the southwestern United States: An abrupt 18.6 ka cold event and evidence for a North Atlantic forcing of Termination I. Quaternary Science Reviews, 30(27–28), 3803–3811. https://doi.org/10.1016/j.quascirev.2011.09.022

Lachniet, M. S., Asmerom, Y., Polyak, V., & Denniston, R. (2020). Great Basin Paleoclimate and Aridity Linked to Arctic Warming and Tropical Pacific Sea Surface Temperatures. Paleoceanography and Paleoclimatology, 35(7). https://doi.org/10.1029/2019PA003785

Lachniet, M., Asmerom, Y., Polyak, V., & Denniston, R. (2017). Arctic cryosphere and Milankovitch forcing of Great Basin paleoclimate. Scientific Reports, 7(1), 1–10. https://doi.org/10.1038/s41598-017-13279-2

Leonard, E. M., Staab, P., & Weaver, S. G. (2005). Kinematics of Spruce Creek rock glacier, Colorado, USA. Journal of Glaciology, 51(173), 259–268. https://doi.org/10.3189/172756505781829403

Lewińska, P., Głowacki, O., Moskalik, M., & Smith, W. A. P. (2021). Evaluation of structure-from-motion for analysis of small-scale glacier dynamics. Measurement, 168(May 2020). https://doi.org/10.1016/j.measurement.2020.108327

Licciardi, J. M., & Pierce, K. L. (2008). Cosmogenic exposure-age chronologies of Pinedale and Bull Lake glaciations in greater Yellowstone and the Teton Range, USA. Quaternary Science Reviews, 27, 814–831. https://doi.org/10.1016/j.quascirev.2007.12.005

Lifton, N., Sato, T., & Dunai, T. J. (2014). Scaling in situ cosmogenic nuclide production rates using analytical approximations to atmospheric cosmic-ray fluxes. Earth and Planetary Science Letters, 386, 149–160. https://doi.org/10.1016/j.epsl.2013.10.052

Lifton, N., Caffee, M., Finkel, R., Marrero, S., Nishiizumi, K., Phillips, F. M., Goehring, B., Gosse, J., Stone, J., Schaefer, J., Theriault, B., Jull, A. J. T., & Fifield, K. (2015). In situ cosmogenic nuclide production rate calibration for the CRONUS-Earth project from lake Bonneville, Utah, shoreline features. Quaternary Geochronology, 26(1), 56-69. https://doi.org/10.1016/j.quageo.2014.11.002

Liu, L., Millar, C. I., Westfall, R. D., & Zebker, H. A. (2013). Surface motion of active rock glaciers in the Sierra Nevada, California, USA: Inventory and a case study using InSAR. Cryosphere, 7(4), 1109–1119. https://doi.org/10.5194/tc-7-1109-2013

Lora, J. M., & Ibarra, D. E. (2019). The North American hydrologic cycle through the last deglaciation. Quaternary Science Reviews, 226, 105991. https://doi.org/10.1016/j.quascirev.2019.105991

Manfreda, S., Dvorak, P., Mullerova, J., Herban, S., Vuono, P., Justel, J. J. A., & Perks, M. (2019). Assessing the accuracy of digital surface models derived from optical imagery acquired with unmanned aerial systems. Drones, 3(1), 1–14. https://doi.org/10.3390/drones3010015

Marcott, S. A., Clark, P. U., Shakun, J. D., Brook, E. J., Davis, P. T., & Caffee, M. W. (2019). 10Be age constraints on latest Pleistocene and Holocene cirque glaciation across the western United States. Climate and Atmospheric Science, 2(1), 1–7. https://doi.org/10.1038/s41612-019-0062-z

Martin, L. C. P., Blard, P. H., Lavé, J., Jomelli, V., Charreau, J., Condom, T., Lupker, M., Arnold, M., Aumaître, G., Bourlès, D. L., & Keddadouche, K. (2020). Antarctic-like temperature variations in the Tropical Andes recorded by glaciers and lakes during the last deglaciation. Quaternary Science Reviews, 247. https://doi.org/10.1016/j.quascirev.2020.106542

Martínez-Carricondo, P., Agüera-Vega, F., Carvajal-Ramírez, F., Mesas-Carrascosa, F. J., García-Ferrer, A., & Pérez-Porras, F. J. (2018). Assessment of UAV-photogrammetric mapping accuracy based on variation of ground control points. International Journal of Applied Earth Observation and Geoinformation, 72(May), 1–10. https://doi.org/10.1016/j.jag.2018.05.015

Masarik, J., and Beer, J. (2009), An updated simulation of particle fluxes and cosmogenic nuclide production in the Earth's atmosphere, J. Geophys. Res., 114, D11103, doi:10.1029/2008JD010557.

Millar, C. I., & Westfall, R. D. (2019). Geographic, hydrological, and climatic significance of rock glaciers in the Great Basin, USA. Arctic, Antarctic, and Alpine Research, 51(1), 232–249. https://doi.org/10.1080/15230430.2019.1618666

Millar, C. I., & Westfall, R. D. (2019). Geographic, hydrological, and climatic significance of rock glaciers in the Great Basin, USA. Arctic, Antarctic, and Alpine Research, 51(1), 232–249. https://doi.org/10.1080/15230430.2019.1618666

Monnier, S., Camerlynck, C., Rejiba, F., Kinnard, C., Feuillet, T., & Dhemaied, A. (2011). Structure and genesis of the Thabor rock glacier (Northern French Alps) determined from morphological and ground-penetrating radar surveys. Geomorphology, 134(3–4), 269–279. https://doi.org/10.1016/j.geomorph.2011.07.004

Munroe, J. S., & Laabs, B. J. C. (2013). Temporal correspondence between pluvial lake highstands in the southwestern US and Heinrich Event 1. Journal of Quaternary Science, 28(1), 49–58. https://doi.org/10.1002/jqs.2586

Munroe, J. S., & Laabs, B. J. C. (2011). New investigations of Pleistocene glacial and pluvial records in northeastern Nevada. GSA Field Guides, 21(January), 1–25. https://doi.org/10.1130/2011.0021(01)

Munroe, J. S., & Laabs, B. J. C. (2013). Latest Pleistocene history of pluvial Lake Franklin, northeastern Nevada, USA. Bulletin of the Geological Society of America, 125(3–4), 322–342. https://doi.org/10.1130/B30696.1

Munroe, J. S., & Laabs, B. J. C. (2017). Combining radiocarbon and cosmogenic ages to constrain the timing of the last glacial-interglacial transition in the Uinta Mountains, Utah, USA. Geology, 45(2), 171–174.

Munroe, J., Walcott, C., Amidon, W., & Landis, J. (2020). A Top-to-Bottom Luminescence-Based Chronology for the Post-LGM Regression of a Great Basin Pluvial Lake. Quaternary, 3(2), 11. https://doi.org/10.3390/quat3020011

Muzikar, P., Elmore, D., & Granger, D. E. (2003). Accelerator mass spectrometry in geologic research. Bulletin of the Geological Society of America, 115(6), 643–654. https://doi.org/10.1130/0016-7606(2003)115<0643:AMSIGR>2.0.CO;2

Osborn, G., & Bevis, K. (2001). Glaciation in the Great Basin of the western United States. Quaternary Science Reviews, 20(13), 1377–1410. https://doi.org/10.1016/S0277-3791(01)00002-6

Oster, J. L., Montañez, I. P., Santare, L. R., Sharp, W. D., Wong, C., & Cooper, K. M. (2015). Stalagmite records of hydroclimate in central California during termination 1. Quaternary Science Reviews, 127, 199–214. https://doi.org/10.1016/j.quascirev.2015.07.027

Oster, J., Warken, S., Sekhon, N., Arienzo, M., & Lachniet, M. (2019). Speleothem Paleoclimatology for the Caribbean, Central America, and North America. Quaternary, 2(1), 5. https://doi.org/10.3390/quat2010005

Otto-Bliesner, B., Brady, E., Clauzet, G., Thomas, R., Levis, S., & Kathavala, Z. (2006). Last Glacial Maximum and Holocene climate in CCSM3. Climate, 19, 2526–2544.

Oviatt, C. G. (2015). Chronology of Lake Bonneville, 30,000 to 10,000 yr B.P. Quaternary Science Reviews, 110, 166–171. https://doi.org/10.1016/j.quascirev.2014.12.016

Owen, L. A., Finkel, R. C., Minnich, R. A., & Perez, A. E. (2003). Extreme southwestern margin of late Quaternary glaciation in North America: Timing and controls. Geology, 31(8), 729–732. https://doi.org/10.1130/G19561.1

Palacios, D., Stokes, C. R., Phillips, F. M., Clague, J. J., Alcalá-Reygosa, J., Andrés, N., Angel, I., Blard, P. H., Briner, J. P., Hall, B. L., Dahms, D., Hein, A. S., Jomelli, V., Mark, B. G., Martini, M. A., Moreno, P., Riedel, J., Sagredo, E., Stansell, N. D., … Ward, D. J. (2020). The deglaciation of the Americas during the Last Glacial Termination. Earth-Science Reviews, 203(January). https://doi.org/10.1016/j.earscirev.2020.103113

Phillips, F.M., Zreda, M.G., Smith, S.S., Elmore, D., Kubik, P.W. and Sharma, P., 1990. Cosmogenic chlorine-36 chronology for glacial deposits at Bloody Canyon, eastern Sierra Nevada. Science, 248(4962), pp.1529-1532.

Phillips, F. M. (2016). Cosmogenic nuclide data sets from the Sierra Nevada, California, for assessment of nuclide production models: I. Late Pleistocene glacial chronology. Quaternary Geochronology, 35, 119–129. https://doi.org/10.1016/j.quageo.2015.12.003

Pierce, K. L. (2003). Pleistocene glaciations of the Rocky Mountains. Developments in Quaternary Science, 1, 63–76. https://doi.org/10.1016/S1571-0866(03)01004-2

Plummer, M.A., and Phillips, F.M., 2003. A 2-D numerical model of snow/ice energy balance and ice flow for paleoclimatic interpretation of glacial geomorphic features. Quaternary Science Reviews, 22(14), 1389-1406.

Quirk, B. J., Moore, J. R., Laabs, B. J. C., Caffee, M. W., & Plummer, M. A. (2018). Termination II, Last Glacial Maximum, and Lateglacial chronologies and paleoclimate from Big Cottonwood Canyon, Wasatch Mountains, Utah. Bulletin of the Geological Society of America, 130(11–12). https://doi.org/10.1130/B31967.1

Quirk, B. J., Moore, J. R., Laabs, B. J. C., Plummer, M. A., & Caffee, M. W. (2020). Latest Pleistocene glacial and climate history of the Wasatch Range, Utah. Quaternary Science Reviews, 238, 106313. https://doi.org/10.1016/j.quascirev.2020.106313

Rasmussen, S. O., Andersen, K. K., Svensson, A. M., Steffensen, J. P., Vinther, B. M., Clausen, H. B., Siggaard-Andersen, M. L., Johnsen, S. J., Larsen, L. B., Dahl-Jensen, D., Bigler, M., Röthlisberger, R., Fischer, H., Goto-Azuma, K., Hansson, M. E., & Ruth, U. (2006). A new Greenland ice core chronology for the last glacial termination. Journal of Geophysical Research Atmospheres, 111(6), 1–16. https://doi.org/10.1029/2005JD006079

Reheis, M. (1999). Highest pluvial-lake shorelines and Pleistocene climate of the western Great Basin. Quaternary Research, 52(2), 196–205. https://doi.org/10.1006/qres.1999.2064

Reheis, M. C., Adams, K. D., Oviatt, C. G., & Bacon, S. N. (2014). Pluvial lakes in the Great Basin of the western United States-a view from the outcrop. Quaternary Science Reviews, 97, 33–57. https://doi.org/10.1016/j.quascirev.2014.04.012

Reimers, A.C., and Laabs, B.J.C., 2018. Climate change during deglaciation inferred from numerical glacier modeling in the Ruby Mountains, Nevada. Abstracts with Programs, Geological Society of America 50(4), doi: 10.1130/abs/2018NC-31356.

Smith, G. I., & Street-Perrott, F. A. (1983). Pluvial lakes of the western United States. In Late-Quaternary environments of the United States. Vol. 1 (pp. 190–212).

Steen, D. (2015). Water balance modeling and paleoclimate investigation of Pleistocene pluvial Lake Clover, Nevada, USA. Unpublished undergraduate thesis, SUNY Geneseo.

Sulaymonova, V. A., Fuchs, M. C., Gloaguen, R., Möckel, R., Merchel, S., Rudolph, M., & Krbetschek, M. R. (2018). Feldspar flotation as a quartz-purification method in cosmogenic nuclide dating: A case study of fluvial sediments from the Pamir. MethodsX, 5(October 2012), 717–726. https://doi.org/10.1016/j.mex.2018.06.014

Tmušić, G., Manfreda, S., Aasen, H., James, M. R., Gonçalves, G., Ben-Dor, E., Brook, A., Polinova, M., Arranz, J. J., Mészáros, J., Zhuang, R., Johansen, K., Malbeteau, Y., de Lima, I. P., Davids, C., Herban, S., & McCabe, M. F. (2020). Current practices in UAS-based environmental monitoring. Remote Sensing, 12(6), 1–35. https://doi.org/10.3390/rs12061001

Truong, K.T., Laabs, B.J.C., and Lam, J.J., 2014. Climate change during the last glaciation in the northern Great Basin inferred from numerical modeling of glaciers in the Ruby Mountains, northern Nevada. Abstracts with Programs, Geological Society of America 46 (6), p. 557.

Villanueva, J. K. S., & Blanco, A. C. (2019). Optimization of ground control point (GCP) configuration for unmanned aerial vehicle (UAV) survey using structure from motion (SFM). International Archives of the Photogrammetry, Remote Sensing and Spatial Information Sciences - ISPRS Archives, 42, 167–174. https://doi.org/10.5194/isprs-archives-XLII-4-W12-167-2019

Wesnousky, S. G., Briggs, R. W., Caffee, M. W., Ryerson, F. J., Finkel, R. C., & Owen, L. A. (2016). Terrestrial cosmogenic surface exposure dating of glacial and associated landforms in the Ruby Mountains-East Humboldt Range of central Nevada and along the northeastern flank of the Sierra Nevada. Geomorphology, 268, 72–81. https://doi.org/10.1016/j.geomorph.2016.04.027

Zreda, M. G., & Phillips, F. M. (2000). Cosmogenic Nuclide Buildup in Surface Materials. In Quaternary Geochemistry: Methods and Applications (pp. 61–74).

APPENDIX A. NDSU COSMOGENIC NUCIDE EXPOSURE PREPARATORY LAB METHODS

The preparation methodology used in the NDSU Cosmogenic Nuclide Preparation lab was adapted from Laabs et al. (2013). Upon return to the lab, information regarding individual samples is recorded for progress tricking; this includes sample ID, mineralogy, weathering, thickness, and sample site geometry. Sample grain size is reduced to a target grain size of 250 to 500 microns using a jaw crusher and a disk mill. All equipment is cleaned carefully with isopropyl alcohol between each sample. Milled samples are sieved to separate the target fraction from the coarse and fine material. The coarse fraction generally contains polyminerallic grains, while the fine fraction may not withstand necessary chemical treatments. Ensuring that sieves are appropriately and thoroughly cleaned is key to preventing cross-contamination between samples. Sieves are placed in an ultrasonic bath in order to dislodge the majority of remaining grains, and any further grains are manually removed with a dental pick.

The first step in isolating quartz is to remove magnetic grains with a neodymium magnet. One at a time, samples are spread thin over a parchment paper sheet, and the magnet, wrapped in a clean Kimwipe, is passed over the sample until it no longer removes grains. Samples are then bottled and rinsed in order to remove lingering fine material and mica grains. These grains remain suspended long enough to decant them while preserving the sample mass; this is key to expediting subsequent quartz isolation processes. The final mechanical separation method applied to samples is froth flotation, a procedure in which felsic grains are removed by taking advantage of the increased rate at which air bubbles will adhere to their surfaces (Whelan and Brown, 1956). Froth flotation begins with pre-treatment, in which each sample is treated with a 1% hydrofluoric acid (HF) solution. The dilute HF interacts with the mineral surfaces, making

quartz hydrophilic while making felspars and muscovite hydrophobic (Sulaymonova et al., 2018). The etched samples are placed into a container with a small amount of tea tree oil and then agitated with carbonated water, causing hydrophobic minerals to float to the surface as they adhere to CO_2 bubbles while hydrophilic grains sink (Sulaymonova et al., 2018). The feldspar and mica grains' pitted surfaces capture CO_2 bubbles and float to the surface, and these grains can then be decanted off, leaving behind a fraction of nearly pure quartz (Sulaymonova et al., 2018). After the completion of froth flotation, the samples are approximately 90-99% pure quartz.

HCl etching bleaches the quartz grain surfaces and removes Fe-oxide coatings, with each sample needing between 4-5 etches before progressing to HF. HF etching with dilute HNO_3 targets lingering feldspar and mica grains removes any meteoric Be from grain surfaces and reduces grain size to ensure no polymineralic grains remain. The strength of the HF and HNO_3 solution is determined based on sample mass to preserve as much quartz as possible. To ensure that the samples are through with HF etching and are ready for AMS preparation, they must pass a dissolution test. A small portion (0.25 grams) of each sample is dissolved in a solution of 99% hydrofluoric acid and 1% sulfuric acid. Dissolved samples are dried in a laminar flow box for approximately 8-12 hours. Samples will either dry to a clear bead or a solid, while those which dry to a solid contain material other than quartz and must be etched further.

Once the samples have all passed the purity test, then chemical preparation for AMS analysis may begin. Beginning with pure crystalline quarts, we must chemically isolate Be in the form of BeO. This is accomplished through a series of chemical conversions and column chromatography. First, an appropriate mass of each sample is determined based on the estimated individual production rate, and then each sample is spiked with a commercial ^{9}Be carrier

solution. Each batch of samples is prepared with a procedural blank, consisting of the ^{9}Be carrier solution and an Al carrier solution. Prepared samples are then dissolved in a proportionate volume of concentrated HF. Once fully dissolved, 3 mL of 6M HCl and 1 mL of 8 M HNO_3 are added to each sample, and they are set to dry in a laminar flow box. At this point, the sample has dried to a solid and is comprised of metal chloride and fluoride salts, the addition of 25 mL of 6 M HCl and subsequent laminar drying will convert the samples to solely chlorides.

Dried samples are once again dissolved in 6 mL of 6 M HCl and are now ready for separation using anion exchange columns. These are columns of an organic resin that allows for the separation of Fe and Ti from the sample. Vials that now contain the sample Be, Al, and Ti in a 6M HCl solution are dried with 1 mL 0.5M H_2SO_4 to convert samples to sulfate form. Repeated addition of 2% H_2O_2 and 1% H_2SO_4 and drying will complete the sulfate conversion and remove organic compounds leached from the anion columns. Samples are now passed through cation exchange columns in order to separate Be, Al, and Ti fractions from one another. The Be fraction is dried in the laminar flow box to a small, nonvolatile bead of liquid. At this point, the sample is ready for precipitation of beryllium hydroxide. Samples are brought to a pH of approximately 8.5 by slow addition of ammonium hydroxide; at this pH, $Be(OH)_2$ will be free to precipitate. The solution will become cloudy as the $Be(OH)_2$ precipitates and vails must be centrifuged to remove the remaining liquid from the gel precipitate. The final step in AMS preparation is to transfer the samples to low-boron quartz vials and then dry and oxidize the $Be(OH)_2$ to BeO by ignition over a Bunsen burner. Isolated BeO can then be loaded into cathodes and then shipped to the AMS facilities at the Purdue PRIME lab.

APPENDIX B. COSMOGENIC NUCLIDE EXPOSURE DATING TABLES AND FIGURES

Table B1. Input data for cosmogenic ^{10}Be surface exposure age calculation

Sample Name	Lat. (DD)	Long. (DD)	Elev. (masl)	Elev./Press. Flag	Thickness (cm)	Density (g/cm^3)	Shielding Correction	Erosion Rate (cm/yr)	[^{10}Be] (atoms/g)	± (atom /g)
Baker Creek Valley										
Terminal										
BC17-02	38.97359	-114.2585	2624	std	2	2.65	0.9943	0	5.63E+05	1.66E+04
BC17-04	38.97573	-114.27243	2868	std	2	2.65	0.98	0	7.23E+05	2.74E+04
BC17-07	38.97059	-114.2644	2715	std	2	2.65	0.98	0	6.54E+05	2.25E+04
BC17-08	38.97057	-114.26456	2726	std	2	2.65	0.98	0	6.04E+05	2.46E+04
BC17-10	38.97153	-114.26031	2680	std	2	2.65	0.947	0	5.63E+05	1.85E+04
BC17-11	38.9719	-114.25942	2662	std	2	2.65	0.97	0	5.95E+05	1.66E+04
BC17-12	38.97174	-114.2589	2645	std	2	2.65	0.97	0	5.99E+05	2.17E+04
BC17-13	38.97192	-114.25864	2648	std	2	2.65	0.97	0	5.02E+05	1.60E+04
BC17-14	38.97234	-114.25714	2618	std	2	2.65	0.96	0	5.78E+05	1.93E+04
BC17-15	38.97226	-114.2569	2610	std	2	2.65	0.97	0	5.68E+05	2.13E+04
Recessional										
BC18-01	38.9668	-114.288	2928	std	1.5	2.7	0.974	0	4.74E+05	1.70E+04
BC18-02	38.9663	-114.289	2949	std	1.5	2.7	0.97585	0	4.10E+05	2.01E+04
BC18-03	38.9664	-114.288	2944	std	1.5	2.7	0.972	0	4.88E+05	4.86E+04
BC18-04	38.9659	-114.289	2960	std	1.5	2.7	0.9771	0	4.45E+05	2.70E+04
BC18-05	38.966	-114.29	2965	std	1.5	2.7	0.9759	0	4.56E+05	3.39E+04
BC18-06	38.9659	-114.289	2949	std	1.5	2.7	0.9729	0	4.86E+05	2.38E+04

Table B2. Cosmogenic ^{10}Be surface exposure age results using the Version 3 online calculator from Balco et al, 2008

Sample Name	*Global 2016 ^{10}Be Production Rate*					*Lifton et al. (2015) Promontory Point ^{10}Be Production Rate*				
Baker Creek Valley	LSDn Age	Int. Uncert.	Ext. Uncert.	LDSn Age	Int. Uncert.	PP-LSDn Age	Int. Uncert.	Ext. Uncert.	PP-LDSn Age	Int. Uncert.
Terminal	(yr)	(yr)	(yr)	(ka)	(ka)	(yr)	(yr)	(yr)	(ka)	(ka)
BC17-02	20805	617	1379	20.1	0.6	20243	600	973	20.2	0.6
BC17-04	22710	866	1602	22.7	0.9	22090	842	1187	22.1	0.8
BC17-07	22734	787	1562	22.7	0.8	22111	765	1134	22.1	0.8
BC17-08	21100	864	1521	21.1	0.9	20541	841	1145	20.5	0.8
BC17-10	20999	694	1426	21.0	0.7	20441	675	1027	20.4	0.7
BC17-11	21783	611	1429	21.8	0.6	21224	595	1000	21.2	0.6
BC17-12	22118	806	1540	22.1	0.8	21551	785	1132	21.6	0.8
BC17-13	18927	606	1275	18.9	0.6	18399	589	912	18.4	0.6
BC17-14	21984	738	1499	22.0	0.7	21422	719	1084	21.4	0.7
BC17-15	21579	814	1517	21.6	0.8	21017	792	1123	21.0	0.8
			Average ± St. Dev.	21.4	1.1			*Average ± St. Dev.*	20.1	1.0
		Average ± St. Dev. Without BC17-13		21.7	0.8		*Average ± St. Dev. Without BC17-13*		21.2	0.7
Recessional										
BC18-01	15065	542	1044	15.1	0.5	14672	528	766	14.7	0.5
BC18-02	12847	632	989	12.8	0.6	12275	604	761	12.3	0.6
BC18-03	15342	1534	1783	15.3	1.5	14937	1493	1596	14.9	1.5
BC18-04	13906	847	1181	13.9	0.8	13438	818	963	13.4	0.8
BC18-05	14211	1060	1354	14.2	1.0	13759	1026	1151	13.8	1.0
BC18-06	15228	749	1172	15.2	0.7	14838	729	920	14.8	0.7
			Average ± St. Dev.	14.4	0.9			*Average ± St. Dev.*	14.0	1.0

Ages calculated with LSDn (Lifton-Sato-Dunai nuclide dependent) (Lifton et al., 2014) scaling scheme, using both global and Promontory Point, Utah production rate calibration datasets from Borchers et al. (2016) and Lifton et al. (2015) respectively)

APPENDIX C. WATER BALANCE LAKE MODELING RESULTS

Lake Clover

Table C1. Results of Lake Clover water balance modeling

CapaS: 140 mm

Temperature Depression (°C)	1725 m (19 ka)	1725 m (17.5 ka)	1725 m (16 ka)	1717 m (14.5 ka)	1720 m (14 ka)	1713 m (12 ka)	1715 m (11.5 ka)	1712 m (9.5 ka)
0.0	0.8811	0.8853	0.8896	0.8341	0.8625	0.8008	0.8206	0.7892
-3.0	0.6935	0.6974	0.7009	0.6534	0.6775	0.6265	0.6441	0.6164
-6.0	0.5969	0.6021	0.6075	0.5492	0.578	0.5174	0.5389	0.5049
-9.0	0.4876	0.49	0.4931	0.469	0.4817	0.4522	0.4642	0.4458

CapaS: 2400 mm

Temperature Depression (°C)	1725 m (19 ka)	1725 m (17.5 ka)	1725 m (16 ka)	1717 m (14.5 ka)	1720 m (14 ka)	1713 m (12 ka)	1715 m (11.5 ka)	1712 m (9.5 ka)
0.0	1.972	1.989	2.01	1.943	1.989	1.898	1.948	1.877
-3.0	1.636	1.651	1.67	1.618	1.657	1.587	1.626	1.57
-6.0	1.424	1.438	1.455	1.411	1.445	1.382	1.419	1.369
-9.0	1.1	1.113	1.129	1.092	1.12	1.071	1.1	1.059

CapaS: 7100 mm

Temperature Depression (°C)	1725 m (19 ka)	1725 m (17.5 ka)	1725 m (16 ka)	1717 m (14.5 ka)	1720 m (14 ka)	1713 m (12 ka)	1715 m (11.5 ka)	1712 m (9.5 ka)
0.0	2.295	2.314	2.336	2.284	2.325	2.254	2.298	2.235
-3.0	1.928	1.945	1.967	1.932	1.964	1.916	1.948	1.904
-6.0	1.72	1.736	1.755	1.724	1.753	1.709	1.74	1.7
-9.0	1.334	1.348	1.365	1.35	1.371	1.347	1.369	1.341

Values within the table represent the factor by which precipitation would need to be multiplied for each temperature depression at each shoreline elevation.

Lake Franklin

Table C2. Results of Lake Franklin water balance modeling

CapaS: 95 mm

Temperature Depression (°C)	1830 m (20 ka)	1850 m (17 ka)	1843 m (15 ka)
0.0	0.5493	0.8855	0.804
-3.0	0.443	0.7333	0.6674
-6.0	0.3961	0.6301	0.575
-9.0	0.3084	0.4945	0.4522

CapaS: 340 mm

Temperature Depression (°C)	1830 m (20 ka)	1850 m (17 ka)	1843 m (15 ka)
0.0	1.218	1.418	1.397
-3.0	0.9825	1.133	1.116
-6.0	0.811	0.923	0.9087
-9.0	0.7106	0.8273	0.8136

CapaS: 3700 mm

Temperature Depression (°C)	1830 m (20 ka)	1850 m (17 ka)	1843 m (15 ka)
0.0	1.824	2.041	2.035
-3.0	1.539	1.716	1.715
-6.0	1.333	1.481	1.484
-9.0	1.059	1.18	1.183

Values within the table represent the factor by which precipitation would need to be multiplied for each temperature depression at each shoreline elevation.

Glacial Modeling

Table C3. Results from glacial modeling of Seitz Canyon, Overland Creek, and Angel Lake (Troung, 2014; Reimers, 2016; Johnson, 2015)

Seitz Canyon (Troung, 2014)

Temperature Depression (°C)	Terminal (20 ka)	Recessional 1 (20 ka)	Recessional 2 (17-15 ka)
-7.5	-	-	2.0
-8.0	-	2.0	-
-8.5	2.0	1.85	1.5
-9.0	1.75	1.6	1.25
-9.5	1.5	-	-
-10.0	-	-	-
-10.5	-	1.0	0.8

Overland Creek (Reimers, 2016)

Temperature Depression (°C)	Terminal (19.9 ka)	Recessional 1 (16.2 ka)	Recessional 2 (14.7 m)	Recessional 3 (13.2 ka)
-6.0	-	-	2.5	1.9
-7.0	2.7	2.5	1.6	1.3
-8.0	1.8	1.6	0.9	0.6
-9.0	1.1	1.0	0.5	-
-10.0	0.7	0.5	-	-
-11.0	0.4	0.3	-	-

Angel Lake (Johnson, 2015)

Temperature Depression (°C)	Recessional 3 (11 ka)
-3.1	3.0
-4.7	2.0
-7.1	1.0
-7.6	0.75
-9.2	0.5

APPENDIX D. UAS SURVEY MODEL AND EXTENDED COMPARATIVE RESULTS

Table D1. Agisoft modeling inputs and position errors

Image Set	Number of Images	Number of Control Points	Number of Control Point Projections	Average Image Position Error (m)	Average Control Point Position Error (m)
2018 Field Season					
Vertical					
18V	259	16*	105	N/A	0.5
2019 Field Season					
Vertical					
19V1	88	16	77	10.3	0.5
19V2	90	16	62	9.0	0.5
Oblique					
19O	104	16	71	11.5	0.5
Vertical + Oblique					
19V1O	192	16	74	10.8	0.5
19V2O	194	16	102	10.3	0.5

Each model was first aligned with accuracy set to “High” and then depth maps were created with quality set to “Medium”.

Current Conditions as of Friday 2021-02-05 10:15 PST										
Time	*Wind*	*Gusts*	*Temp*	*Precip Prob*	*Cloud Cover*	*Visibility*	*Visible Sats*	*Kp*	*Est. Sats Locked*	*Good To Fly?*
10:15 ☼	13 mph↘	28 mph↘	31°F	-	2%	16 km	11	1	10.9	no

Friday 2021-02-05: sunrise 06:39, sunset 17:02										
Time	*Wind*	*Gusts*	*Temp*	*Precip Prob*	*Cloud Cover*	*Visibility*	*Visible Sats*	*Kp*	*Est. Sats Locked*	*Good To Fly?*
11:00 ☼	12 mph↘	28 mph↘	34°F	-	10%	16 km	13	1	12.9	no
12:00 ☼	16 mph↘	33 mph↘	35°F	4%	23%	16 km	14	1	13.8	no
13:00 ☼	17 mph↘	33 mph↘	35°F	-	23%	16 km	19	1	18.8	no
14:00 ☼	16 mph↘	30 mph↘	36°F	5%	20%	16 km	21	1	20.6	no
15:00 ☼	16 mph↘	27 mph↘	33°F	-	11%	16 km	19	1	18.6	no
16:00 ☼	16 mph↘	27 mph↘	30°F	-	14%	16 km	15	2	15.0	no
17:00 ☾	12 mph↘	19 mph↘	25°F	5%	10%	16 km	15	2	15.0	no
18:00 ☾	12 mph↘	18 mph↘	23°F	4%	6%	16 km	14	2	13.7	no
19:00 ☾	11 mph↘	15 mph↘	22°F	-	2%	16 km	13	2	12.0	no
20:00 ☾	10 mph↘	13 mph↘	21°F	1%	1%	16 km	12	2	10.6	no
21:00 ☾	10 mph↘	13 mph↘	20°F	1%	2%	16 km	11	2	9.6	no
22:00 ☾	10 mph↘	11 mph↘	20°F	-	2%	16 km	13	1	11.3	no
23:00 ☾	9 mph↘	10 mph↘	19°F	-	2%	16 km	11	1	10.1	no

Figure D1. Example of forecasting available from UAVforecast™ for the approximate location of the Wheeler Peak rock glacier cirque

Figure D2. 2018 Vertical image set survey statistics

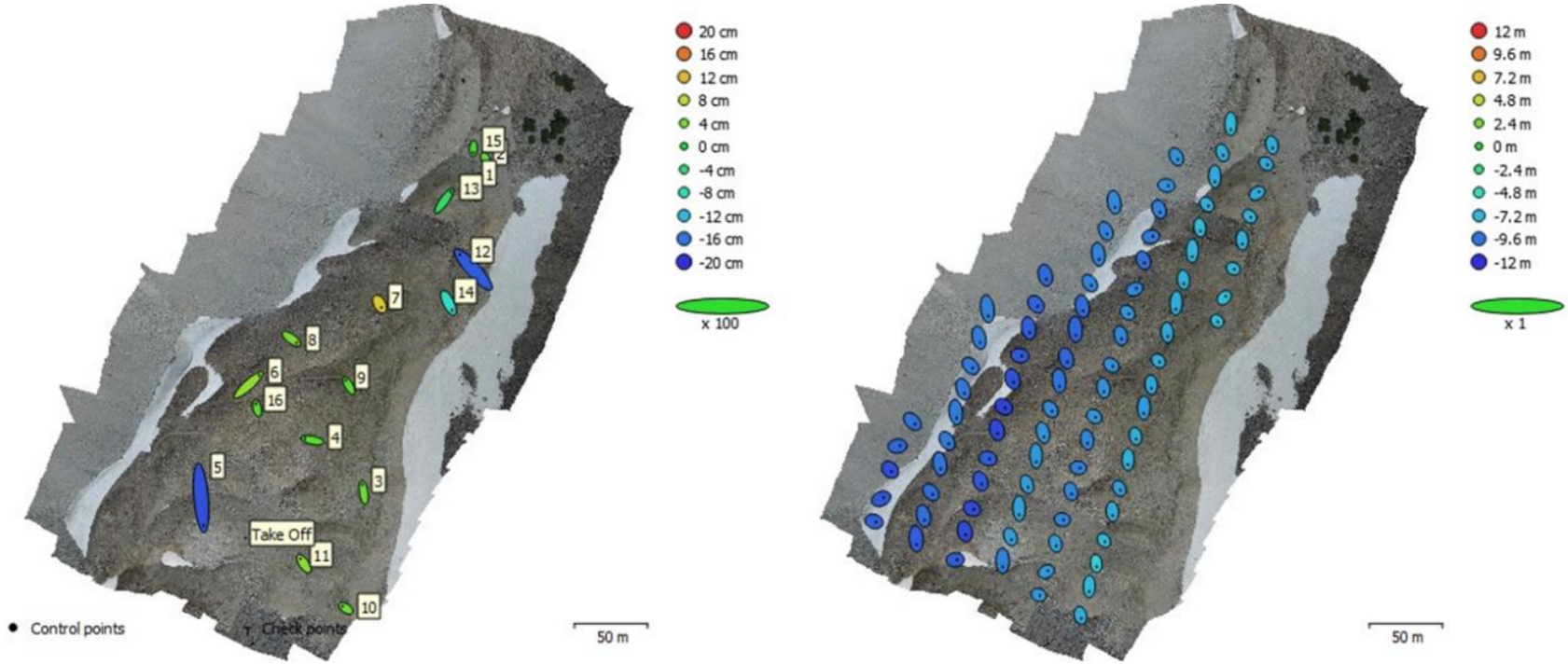

Figure D3. 2019 Vertical 1 image set survey statistics

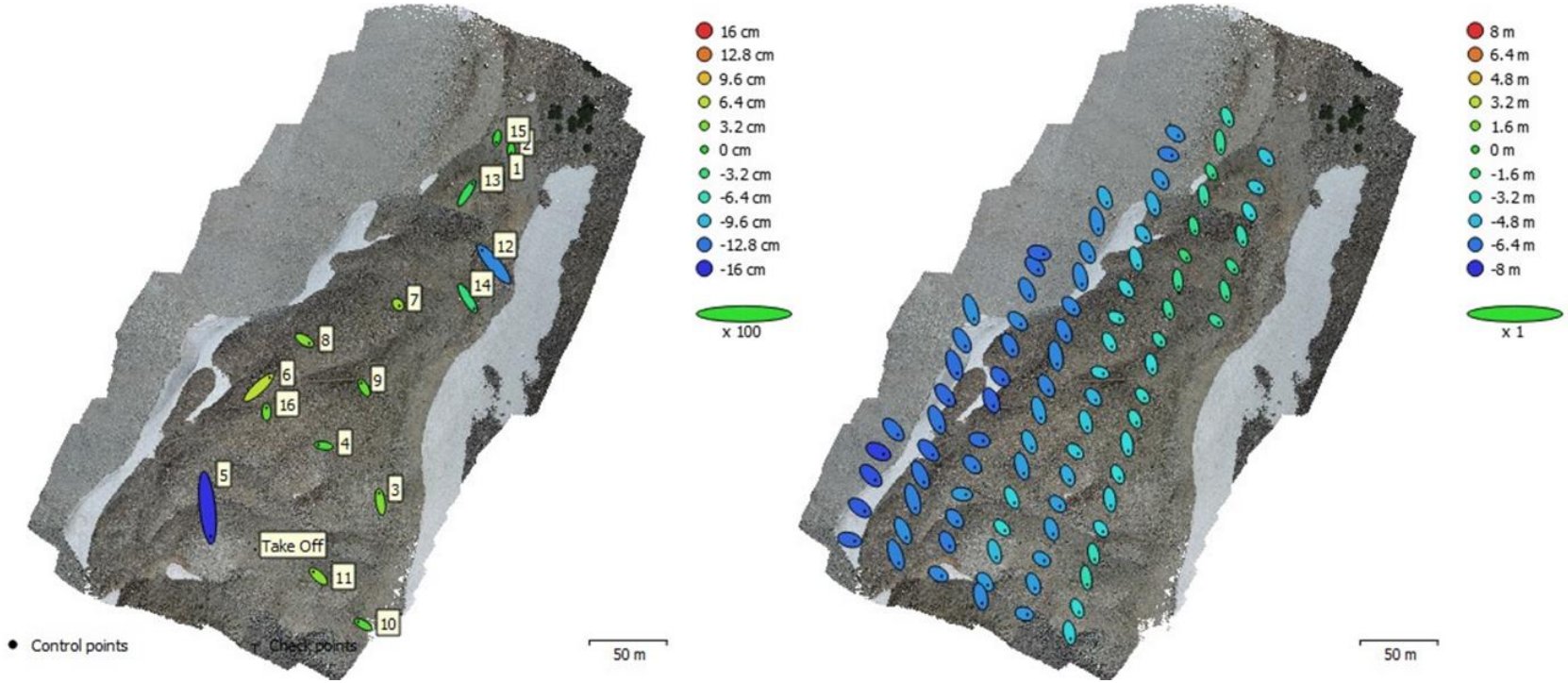

Figure D4. 2019 Vertical 2 image set survey statistics

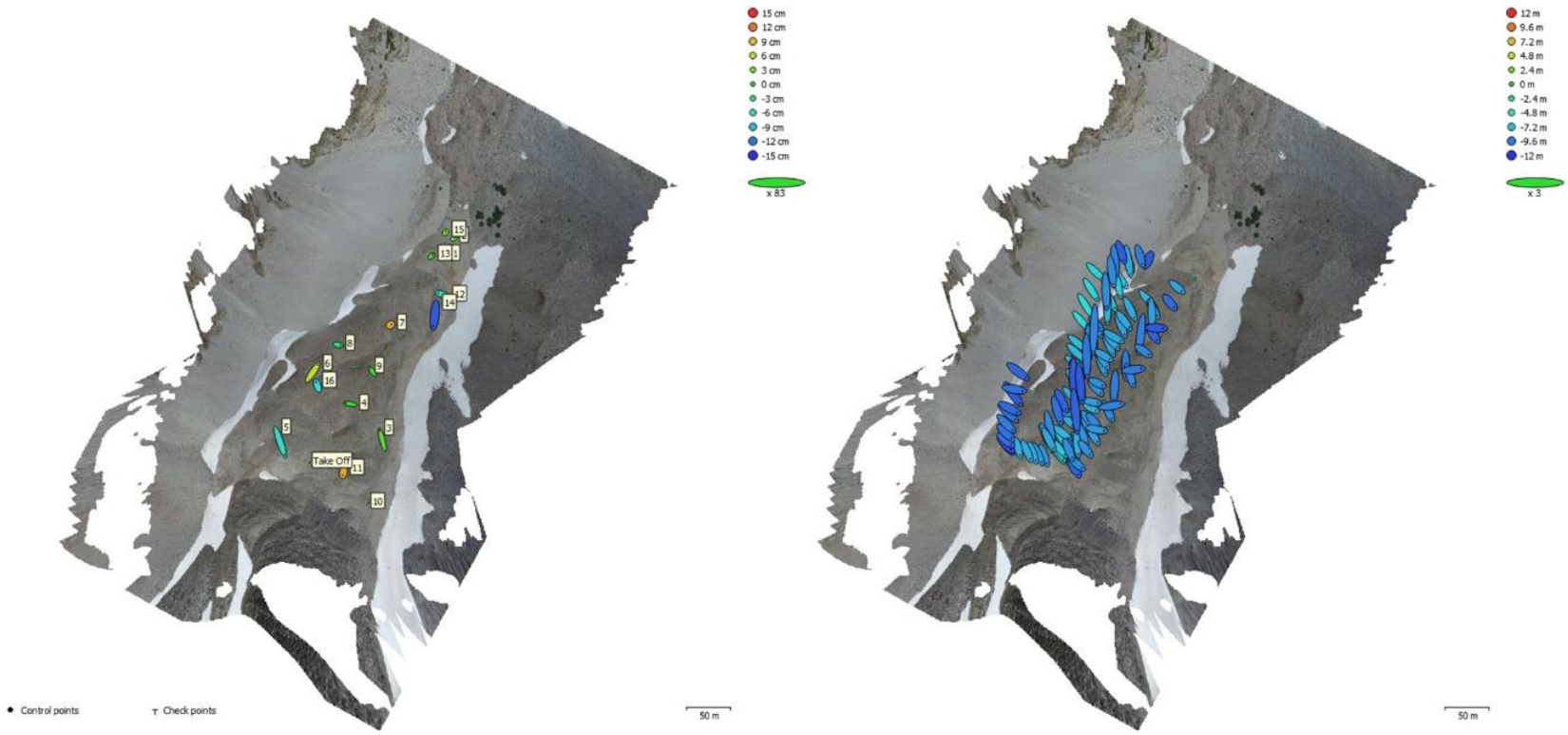

Figure D5. 2019 Oblique image set survey statistics

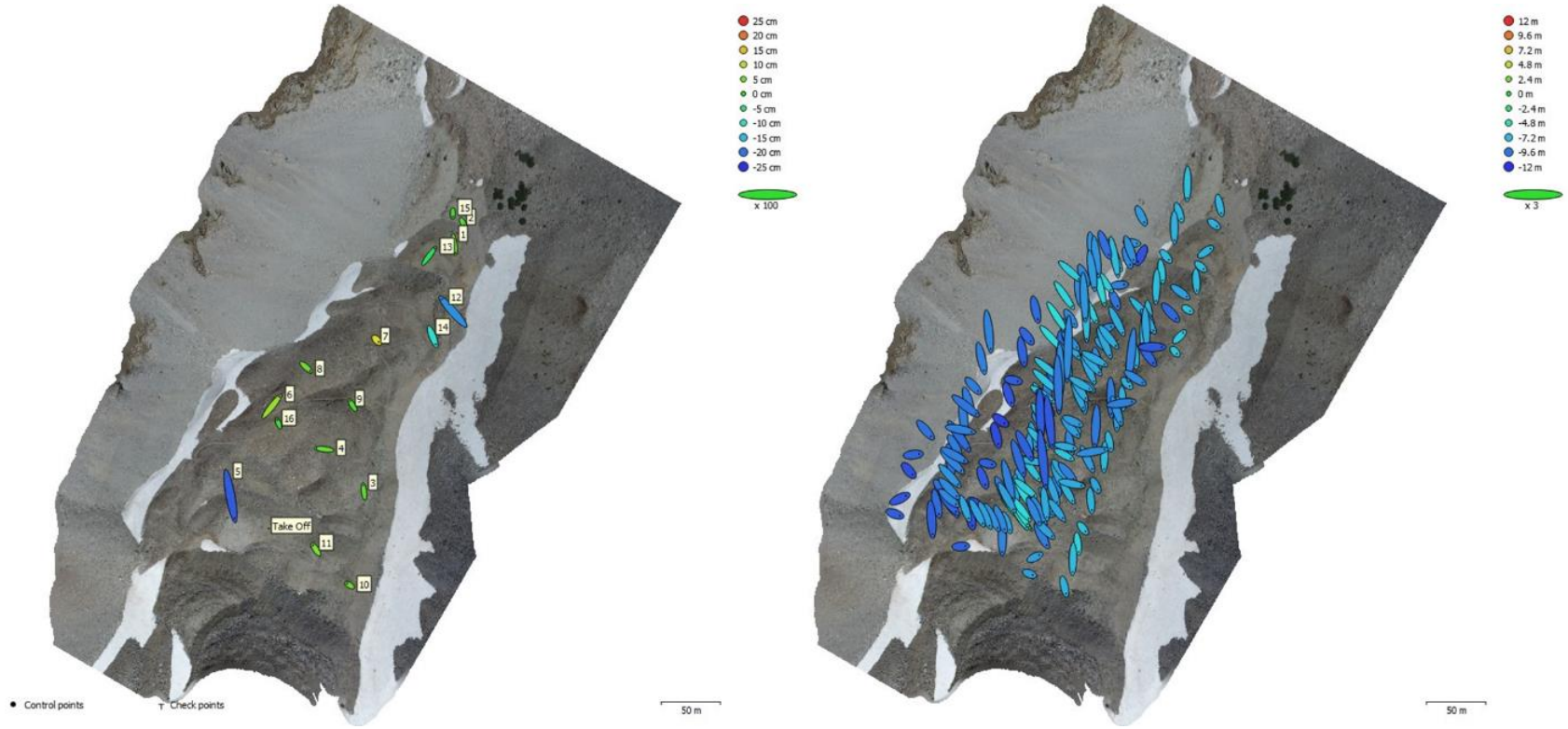

Figure D6. 2019 Vertical 1 plus Oblique image set survey statistics

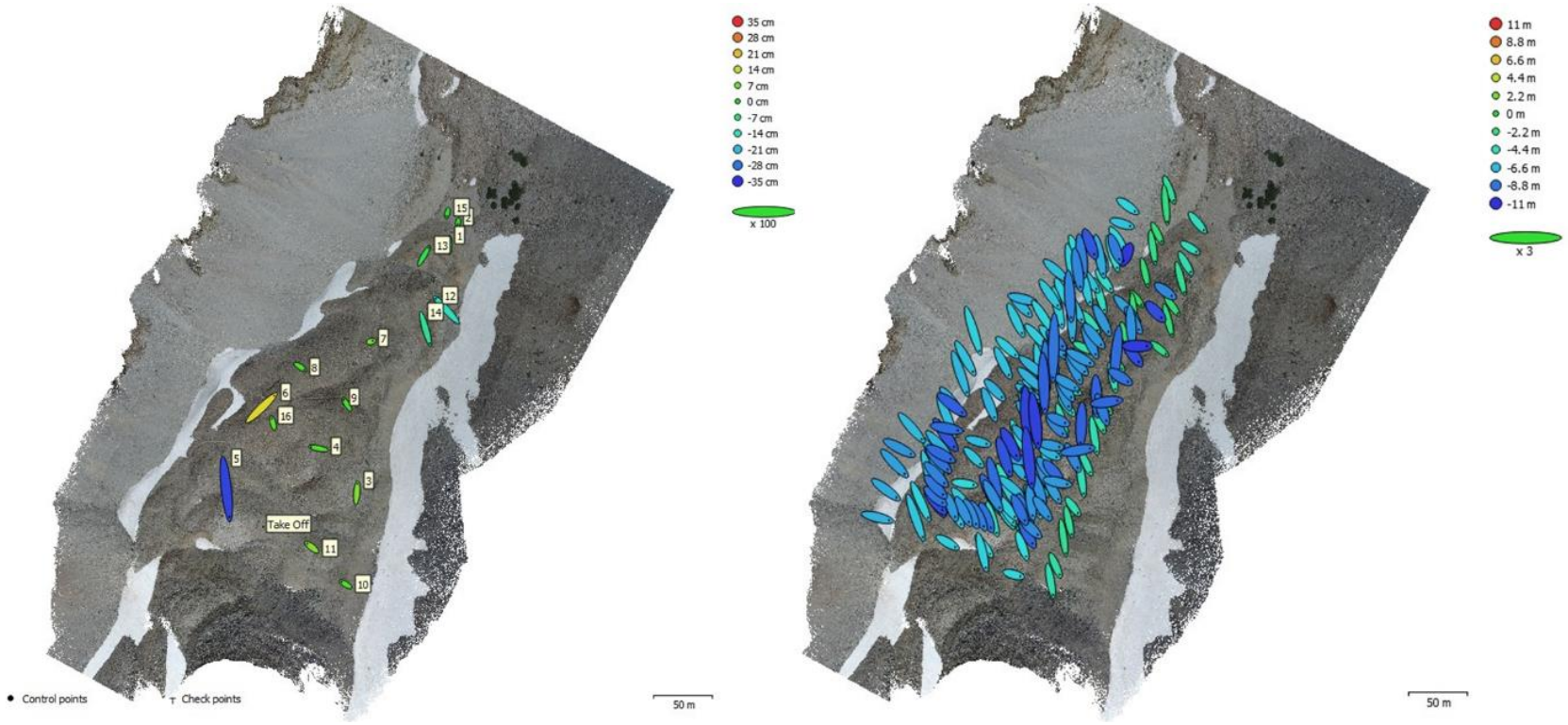

Figure D7. 2019 Vertical 2 plus Oblique image set survey statistics